The DOI for this manuscript is doi: 10.1175/JAS-D-16-0075.1

The final published version of this manuscript will replace the preliminary version at the above DOI once it is available.

If you would like to cite this EOR in a separate work, please use the following full citation:

Chang, C., and C. Wu, 2017: On the Processes Leading to the Rapid Intensification of Typhoon Megi (2010). J. Atmos. Sci. doi:10.1175/JAS-D-16-0075.1, in press.

On the Processes Leading to the Rapid Intensification of Typhoon Megi (2010)

Chuan-Chieh Chang and Chun-Chieh Wu

Department of Atmospheric Sciences, National Taiwan University, Taipei, Taiwan

Submitted to Journal of the Atmospheric Sciences

(Revised on 30 December, 2016)

*Corresponding author address: Chun-Chieh Wu, Department of Atmospheric Sciences, National Taiwan University, No. 1, Sec. 4, Roosevelt Rd., Taipei 10617, Taiwan. E-mail: cwu@typhoon.as.ntu.edu.tw

Abstract

The processes leading to the rapid intensification (RI) of Typhoon Megi (2010) are explored with the convection-permitting full-physics model and a sensitivity experiment using different microphysical scheme. It is found that the temporary active convection, gradually-strengthened primary circulation and a warm core developing at mid level tend to serve as precursors prior to RI. The potential vorticity (PV) budget and Sawyer-Eliassen model are utilized to examine the causes and effects of those precursors. Results show that the secondary circulation, triggered by the latent heat associated with active convection, acts to strengthen the mid-upper-level primary circulation by transporting the larger momentum toward the upper layers. The increased inertial stability at mid-upper level not only increases the heating efficiency but also prevents the warm-core structure from being disrupted by the ventilation effect. The warming above 5 km effectively lowers the surface pressure.

It is identified that the strong secondary circulation helps to accomplish the mid-level warming within the eye. The results based on potential temperature (θ) budget suggest that the mean subsidence associated with detrainment of active convection is the major process contributing to the formation of mid-level warm core. On the possible causes triggering the inner-core active convection, it is suggested that the gradually-increased vortex-scale surface enthalpy flux accounts a leading role for the development of vigorous convection. Our results also highlight the potentially dominant role of weak-to-moderate convection on the onset of RI, while the convective bursts play a supporting role. Based on the aforementioned analyses, a schematic diagram is shown to describe the plausible path leading to the RI.

1. Introduction

While tropical cyclone (TC) track forecasts have improved significantly during the past 20 years, the progress in intensity forecasts has been relatively slow, about one-third to one-half in percentage of those track model improvements at 24-72 h forecast (Cangialosi and Franklin 2012; Falvey 2012; DeMaria et al. 2014). TC intensity forecasting remains as a challenging task since TC intensity change is affected by multi-scale processes (Wang and Wu 2004), ranging from synoptic (environmental conditions), vortex, convective, turbulent, to microscales (Marks and Shay 1998). In addition, the operational prediction of rapid intensification (RI) has been shown to be particularly difficult (Elsberry et al. 2007). Unexpected RI episodes could cause serious loss of life and property to the coastal regions, indicating the importance in improving our understanding of the mechanisms leading to RI.

Kaplan and DeMaria (2003, hereafter KD03) used the Statistical Hurricane Intensity Prediction Scheme to investigate the environmental difference between RI and non-RI TCs. Synoptic conditions conducive to RI were identified, including weaker vertical wind shear (VWS), higher relative humidity in the lower troposphere, warmer sea surface temperatures (SSTs), stronger upper-level easterly wind and fewer external forcings like trough systems. Based on the same dataset, it was also found that rapidly-intensifying TCs intensify more rapidly during the 12-h period prior to RI. In KD03, RI was defined when a TC intensifies by more than 30 kt (15.4 m s^{-1}) during a 24-h period. Although the aforementioned environmental conditions were found statistically different between the RI and non-RI cases, some exceptions were also documented. For instance, rapidly-intensifying TCs had been observed and simulated in high VWS environments (Molinari and Vollaro 2010; Nguyen and Molinari 2012; Kanada and Wada 2015), pointing out that these favorable environments are neither necessary nor sufficient conditions for RI. Besides, there are other important forecast and scientific problems related to RI that remain to be fully studied, such as 1) the difference of intensification rate between the slowly- and rapidly-intensifying TCs (Hendricks et al. 2010), and 2) the precise time of RI onset. It is thus important to further investigate the inner-core dynamics and their interaction with the surroundings prior to and during RI.

Earlier theoretical works have emphasized the synergetic interactions between the convective heating and the axisymmetric, overturning circulation related to TC intensification. Secondary circulation triggered by external forcing (latent heat or friction) drives an inward advection of greater angular momentum, resulting in acceleration of swirling winds (e.g., Eliassen 1951; Ooyama 1969; Ooyama 1982; Shapiro and Willoughby 1982). Using a balanced vortex model, Schubert and Hack (1982) and Vigh and Schubert (2009) showed that latent heat located inside the radius of maximum azimuthal mean wind (RMW), where inertial stability [defined as $(f + \frac{2\bar{v}}{r})(f + \frac{\partial(r\bar{v})}{r\partial r})$, where $\bar{V}$ is the azimuthal mean tangential wind and f is the Coriolis parameter] is large, acts to intensify the vortex most efficiently.

Ranging from meso- to convective-scale, both observational and numerical studies have suggested that vortical hot towers or convective bursts (CBs) with cold cloud tops and intense vertical motions near the storm center may play an important role in rapidly-intensifying processes (Heymsfield et al. 2001; Reasor et al. 2009; Guimond et al. 2010; Kelley and Halverson 2011; Zhang and Chen 2012; Chen and Zhang 2013; Rogers et al. 2013; Wang and Wang 2014; Chen and Gopalakrishnan 2015). Using satellite, Doppler radar and in-situ data, Heymsfield et al. (2001) found that the vigorous vortical hot tower, which extends to an altitude of nearly 18 km, can induce mesoscale subsidence in the eye. This subsidence occupied a substantial vertical depth in the eye, and was identified to result in about 3°C warming. Guimond et al. (2010) discovered that intense eyewall updrafts (upward motion greater than 20 m s^{-1}), which are flanked by downdrafts of 10-12 m s^{-1}, are transported toward the eye by 15-20 m s^{-1} inflow over a deep layer (0.5-10 km), followed by the succeeding axisymmetrization of the warm-core structure and a 11-hPa pressure drop in 1 h 35 min. The aforementioned studies indicated that CBs were observed during RI. In addition, CBs had also been detected prior to RI in other observational studies (Stevenson et al. 2014; Rogers et al. 2015; Susca-Lopata et al. 2015). By comparing the inner-core characteristics between intensifying and steady-state hurricanes, Rogers et al. (2013) showed that CBs and latent heat located inside the RMW are important features of intensifying hurricanes, consistent with the theoretical study of Schubert and Hack (1982) and Vigh and Schubert (2009). Recently, numerical studies (Zhang and Chen 2012; Chen and Zhang 2013; Wang and Wang 2014) showed that upper-level warming due to the subsidence of stratospheric air associated with the detrainment of CBs straddling the RMW initiates RI in the simulated Hurricane Wilma (2005) and Typhoon Megi (2010). These numerical and observational studies (e.g., Heymsfield et al. 2001; Guimond et al. 2010; Chen and Zhang 2013; Wang and Wang 2014) suggested a possible mechanism leading to RI. Namely, CBs occurring inside the RMW may create extra latent heat at the place, where there is high inertial stability, and are also accompanied by intense subsidence with high-θ air from stratosphere, which is favorable for the warming aloft in the eye. The minimum surface pressure (MSLP) drop associated with the upper-level warm-core structure is thus conducive to initiate RI.

Some studies indicated that the low-level air in the eye has high equivalent potential temperature (θ_e) and can provide the fuel for intense convection in the eyewall (Montgomery et al. 2006; Barnes and Fuentes 2010; Miyamoto and Takemi 2013; Wang and Wang 2014). Based on the GPS dropwindsonde dataset, Barnes and Fuentes (2010) showed that the difference in θ_e between the eye and eyewall decreases remarkably during the RI period of Hurricane Lili (2002). They hypothesized that the warm-θ_e air in the eye is transported into the eyewall through the eye-eyewall mixing process (e.g., Persing and Montgomery 2003; Cram et al. 2007), stimulating vigorous convection, and thus likely initiates the RI. However, they pointed out that the volume of the eye is small compared with the eyewall, thus the high-θ_e air in the eye couldn't sustain the whole RI episode. Similarly, Wang and Wang (2014) examined the slantwise convective available potential energy (SCAPE) and found that SCAPE decreases significantly with increased CB activity in the eyewall after the RI onset. They considered the CBs to be triggered/supported by the SCAPE in the eye region. Employing an idealized full-physics model, Miyamoto and Takemi (2013) found that the inner-core air parcel would acquire more enthalpy due to the increased axisymmetricity, which actuates the intense convection within the eyewall and strengthens the secondary circulation. Consequently, the reinforced secondary circulation gives rise to the RI onset. Note that there may be an alternative process not directly related to CBs which initiates RI. In the numerical study of Rogers (2010), it was suggested that the onset of RI is linked to an increase of convective precipitation and low-level upward mass flux, but neither the intensity nor the number of CBs seem to be a key for RI. However, Rogers (2010) indicated that CBs located inside the RMW about 6 h prior to RI may play some roles in enhancing the vortex-scale secondary circulation. The enhanced secondary circulation is accompanied by increased PV and inertial stability, which are conducive to the RI onset. Using satellite data, Kieper and Jiang (2012) demonstrated that a ring-like axisymmetric precipitation pattern could be a useful predictor for RI. In addition, Zagrodnik and Jiang (2014) indicated that compared with slowly-intensifying TCs, rapidly-intensifying TCs contain broader precipitation area, especially at the upshear quadrants, and more symmetric rainfall distribution in the inner-core region. The above-mentioned broader precipitation is composed of shallow convection and stratiform precipitation. Meanwhile, the moderate-to-deep convective area increases significantly 12 h after the RI onset. Recently, Tao and Jiang (2015) indicated that moderate-to-deep precipitation contributes less total volumetric rain and latent heat to the inner-core region of rapidly-intensifying storms at the onset of RI, as compared to the slowly-intensifying TCs. They further argued that RI is more likely triggered by widespread shallow-to-moderate precipitation, and that the appearance of more moderate-to-deep precipitation in the middle of RI is more like a response to the strengthening of the vortex.

Given the distinct possible processes to initiate RI presented in aforementioned studies, we are motivated to study the mechanisms leading to RI via a numerical study of Typhoon Megi (2010), and to compare our findings with previous studies (e.g., Wang and Wang 2014). To understand the mechanisms leading to RI, we try to answer the following questions:

1. What are the key features at various scales prior to the RI of Megi?
2. What are the possible causes and/or effects of these precursors to RI?
3. What's the uncertainty of RI with respect to different microphysical processes (e.g., Li and Pu 2008) in the numerical model?

Section 2 describes the experimental design used to perform the control experiment, the sensitivity experiments with different cloud microphysical schemes, the definitions used to distinguish different types of precipitation and identify the storm center, and the synopsis of Megi. The key features, especially at the vortex- to convective-scales prior to RI are presented in section 3. In section 4, the PV budget is conducted, and the Sawyer-Eliassen (SE) model diagnostics (e.g., Eliassen 1951; Shapiro and Willoughby 1982; Hack and Schubert 1986) are adapted to examine the physical links between these precursors. Section 5 compares inner-core evolutions between the control experiment and a sensitivity experiment with different intensification rate. A possible path triggering RI is discussed in section 6.

2. Experimental design

a. Synopsis of Megi

Typhoon Megi (15W) was the strongest and most persistent TC in the Western North Pacific during 2010, developing from the tropical equatorial waves in early October 2010 (Fang and Zhang 2016). A tropical depression was declared by the Joint Typhoon Warning Center (JTWC) and Japan Meteorological Agency (JMA) on 12 October 2010, and it further intensified into a tropical storm, named Megi by JMA at 1200 UTC 12 October. Megi became a category-1 typhoon at 0000 UTC 14 October, and it continued intensifying until 0000 UTC 15 October. However, the intensification stagnated between 0000 UTC 15 and 0000 UTC 16 October. It started intensifying again from 0000 UTC 16 October, and the intensification rate increased to a higher level than that prior to 0000 UTC 15 October. In the meantime, MSLP dropped from 956 to 903 hPa and the peak 10-m winds increased from 90 kt (46 m s^{-1}) to 160 kt (82 m s^{-1}). The second intensification phase started from 0000 UTC 16 October and can be categorized as a case with RI, according to the definition given by KD03.

b. Experimental design and analytical methods

The Weather Research and Forecasting Model (WRF, Version 3.4.0, see Skamarock et al. 2008) is employed to conduct the 4-day simulations initiated at 0000 UTC 15 October, which is about 24 h before the observational onset of RI associated with Megi. Experiments are set up in triple nested domains while the inner two nests are vortex-following (Fig. 2). Each domain has 334×250, 181×181 and 181×181 grid points, with grid spacing of 12, 4 and 1.33 km, respectively. The inner-most domain contains a horizontal areal coverage of 240 km ×240 km, enough to resolve the inner-core region of Megi. Vertical grid meshes include 35 levels in the terrain-following σ coordinates from the surface to 50 hPa, with enhanced vertical resolution below 1-km height and at the outflow layer (z = 14-16 km). The σ coordinates are shown in Appendix C. The initial fields and boundary conditions are derived from National Center for Environmental Prediction final reanalysis field at $1^{\circ}\times1^{\circ}$ resolution. In the coarse grid spacing (12km), Kain-Fritsch cumulus parameterization (Kain and Fritsch, 1993; Kain 2004) is adopted. In all three domains the following parameterization schemes are used: 1) The WRF single moment 6-class microphysics scheme (WSM6; Hong and Lim 2006) with hydrometeor of water vapor, cloud water, rain, snow, graupel and cloud ice; 2) Rapid Radiative Transfer Model (RRTM; Mlawer et al. 1997) for long waves and Dudhia (1989) shortwave radiation scheme; and 3) Yonsei University (YSU) PBL parameterization with the Monin-Obukhov surface layer scheme (Hong et al. 2006). Note that the results associated with the potential temperature (θ) budget and the convective-scale analyses are based on 2-min output, the vortex-scale analyses are based on 10-min output, while the synoptic analyses are based on 1-h output. The highest temporal-resolution (1-min) results are applied in the PV budget.

The approximate geometric center (centroid) of the storm is determined for each analysis based on the horizontal distribution of pressure, similar to Kanada and Wada (2015). The geometric center is calculated at horizontal distances of 1.33 km, and summed within the radius of 90 km from the simulated vortex-tracking center for every grid $(X_{cp\mp25\,grid,}Y_{cp\mp25grid})$ around the location of the CP (X_{cp}, Y_{cp}). The grid (X, Y) at which the summation is the smallest is selected as the storm center. The tilting distance between the low-level pressure geometric center and upper-level pressure geometric center is very small (about 10~15 km, figures not shown), which indicates that errors resulting from the vertical tilting are limited. For the analyses of the budgets, which calculate the vertical advection terms, the fixed surface center is used for the whole column. On top of that, the center varying with height is applied for the other analyses.

c. Sensitivity to cloud microphysical schemes

Li and Pu (2008) demonstrated that the intensification rates of the simulated Hurricane Emily (2005) during its early RI stage were sensitive to the different cloud microphysical schemes. Therefore, it is feasible to evaluate the uncertainty of RI by conducting experiments with various cloud microphysical schemes (listed in Table 1). The complexity of the hydrometeor species in these cloud microphysical schemes is different. The impact of the WRF single moment 3-class (WSM3; Hong et al. 2004) scheme is examined in this study, and is also compared with the control simulation using WSM6 for microphysical scheme (CTRL). In WSM3, three classes of hydrometeors:

water vapor, cloud water - cloud ice, and rain - snow are considered. The ice processes (cloud ice and snow) exist below or equal to 0℃, and the number of ice particles is a function of ice content. When the temperature is above 0℃, cloud water and rain are exhibited.

d. Definitions of RI and different types of precipitation

We modify the convective-stratiform partitioning algorithm based on Rogers (2010), which made certain modifications on the method originally developed by Steiner et al. (1995). CBs, defined by an averaged vertical velocity higher than 5 m s^{-1} between 700-300 hPa, are not included in the convective precipitation. This definition of CB is more similar to that in Reasor et al. (2009). The modified convective region is categorized as "weak-to-moderate convection" in this study. Except for the weak-to-moderate convection, definitions for other types of precipitation are the same as Rogers (2010). Although Rogers (2010) provided a detailed description for the definitions related to the different types of precipitation, the partitioning algorithm given by Rogers (2010) might potentially underestimate the contributions from CBs due to their inherent vertical slope (e.g., Fig. 3 of Harnos and Nesbitt 2016). The shortcomings of the definitions and their possible impacts on the results will be further discussed in section 6.

The definition of RI adopted in this study is that when the maximum surface wind speed increases by more than 30 kt (15.4 m s^{-1}) during a 24-h period (from KD03), which has been widely employed in other studies (e.g., Wang and Wang 2014).

3. Results - features at different scales prior to RI

a. Comparisons with observations

As shown in Fig. 1, the RI of Megi is generally well reproduced by the WRF model. Although the simulated onset of RI commences about 6 h earlier and the simulated peak intensity is 5-7 m s^{-1} weaker than observation, the simulated intensification rate is close to the JTWC best track data (Fig. 1a). Note that the simulated maximum surface wind speed starts intensifying after 1800 UTC 15 October, while the MSLP commences deepening after 2000 UTC 15 October (Fig. 1a), implying that there is an uncertainty associated with the onset time of RI. This uncertainty was also addressed in McFarquhar et al. (2012). 1800 UTC 15 October is defined as the onset time of RI, and all the analyses prior to RI are relative to this time throughout the whole study. It should also be noted that no special initialization scheme or data assimilation is applied here. Therefore, the initial vortex is weaker than the real TC. Nevertheless, the simulated Megi spins up very quickly with sharp reduction in the RMW (Fig. 1b) during the first few hours, and the simulated RMW resembles the observation when RI begins. However, it is worth noting that the central SLP deepens dramatically (~ 20 hPa) with the substantial increase of surface maximum wind (~ 20 m s^{-1}) during the first 1-2 h of the simulation, implying that the first 1-2 h of simulation is the spin-up period. Therefore, most analyses associated with the first 3 h of simulation are omitted in the following study. The comparison between the model-predicted track of Megi and the best-track analysis is shown in Fig. 2. Although there is a southward bias associated with the simulated storm, the model generally well captures the movement of Megi during the 4-day simulation (Fig. 2).

The simulated total graupel mass within the column could serve as a proxy of deep convection for comparison with low-brightness temperature observed by satellite (Spencer et a. 1994; McFarquhar et al. 2012). Figure 3a indicates that the model reproduces the convective asymmetry prior to RI, but there is some radial difference of the simulated location associated with the deep convection. When the simulated Megi reaches its peak intensity, the robust and compact eyewall with RMW of about 20 km is generally captured by the model (Fig. 3c). Meanwhile, the deep convection relatively concentrating in the southern eyewall can be identified both in the observation and simulation (Figs. 3c and 3d). In addition, the simulation is examined by comparing with the intensive observation data acquired during ITOP (Impact of Typhoons on the Ocean in the Pacific, 2010) field program. The radial profiles of flight-level and surface winds between the simulation and the observation are compared. It is shown that the simulated peak winds are slightly weaker than the observed winds at around 2200 UTC 17 October (Figs. 4b and 4c). On the other hand, the simulated wind fields are closer to the observations at 1200 UTC than the simulated results around 2200 UTC 17 October (Figs. 4a and 4c). The weaker simulated wind profiles presented around 2200 UTC 17 October may be attributed to an unrealistic eyewall replacement process in the simulation (figure not shown), which occurs after the simulated Megi reaches its peak intensity. This unrealistic eyewall replacement process probably hinders further intensification of the simulated Megi. Nevertheless, previous comparisons between the simulation and the observation demonstrate that the model-predicted results reasonably reproduce the intensification process of Megi. Therefore, these results could provide a prospective basis for further exploration that is helpful to understand the factors responsible for the RI of Megi.

b. Synoptic environment

Prior to the onset of RI, the thermodynamic environmental conditions, including the high SSTs and the moist lower troposphere (Table. 2), are beneficial to RI, as suggested by the previous statistical studies (KD03; Kaplan et al. 2010). However, the large scale dynamic patterns are more complicated than those thermodynamic conditions. Namely, the larger upper-level divergence and smaller relative eddy flux convergence (REFC) are favorable environmental conditions for RI as identified by KD03 (Table. 2). In contrast to these conditions, the simulated mean VWS exceeds 8 m s^{-1} (Table. 2), which is detrimental for TC intensification, and the VWS further increases 6 h prior to RI. Although the VWS decreases slightly by 1600 UTC 15 October, the magnitude of decrease (~0.5 m s^{-1}) is pretty small, as compared with the amplitude of increase 6 h prior to RI (~5 m s^{-1}). This suggests that the decreasing shear could not be the factor leading to the RI. In all, the environmental conditions prior to RI is somewhat mixed for TC intensification. Hence, the inner-core processes likely play a crucial role in initiating RI.

c. Vortex-scale evolution

During 0000 UTC and 0500 UTC 15 October, the surface RMW of the simulated Megi decreases considerably from about 100 km to less than 50 km (Fig. 1b). This considerable reduction of RMW may be linked to the spin-up stage of the simulation, which is ascribed to the unrealistic initial storm structure in the final analysis data. The RMW undergoes large fluctuations from 0600 UTC to 1200 UTC 15 October, which may be related to the transient development of the mesoscale convective system near the TC center (Figs. 1b, 5a and 8a). The contraction of vortex during 0500 UTC to 0700 UTC 15 October is rather asymmetric (figure not shown), implying that the relatively weak background vortex is affected by the temporally active convection. During the succeeding 6 h prior to RI, the fluctuation of surface RMW gradually diminishes (Fig.

1b). Consistent with the result of Wang and Wang (2014), but different from other numerical studies (e.g., Fig. 1b of Chen and Gopalakrishnan 2015), the contraction of simulated RMW during RI is relatively insignificant (Fig. 1b). Furthermore, both the tangential wind and the radial wind strengthen before the RI commences (Fig. 5a), supporting the statement made by Rogers (2010) that the enhanced primary circulation and secondary circulation could be the precursors responsible for RI. It is worth noting that the sudden development of convective system near the TC center precedes the intensification of the primary circulation (Fig. 5a), suggesting that the development of temporary convective system may be conducive to the spin-up of the initial weak TC vortex via strengthening of the storm-scale secondary circulation.

In this study, the radius of 80 km serves as an estimate of the inner-core size since it covers most of the grid points inside the RMW and its azimuthal mean tangential wind approximates to the damaging-force wind (25.7 m s^{-1}) that is used to define the inner-core size in Knaff et al. (2007) and Xu and Wang (2010). Therefore, most of the analyses are conducted inside the radius of 80 km.

In addition to the azimuthal mean tangential wind, PV, inertial stability and axisymmetricity (e.g., Miyamoto and Takemi 2013; Wang and Wang 2014) can also serve as important dynamical parameters for describing vortex-structure evolutions. Here, same as in Miyamoto and Takemi (2013), the axisymmetricity is defined as:

$$A_{ut}(r,z,t) \equiv \frac{\bar{A}^{\lambda}(r,z,t)^2}{\bar{A}^{\lambda}(r,z,t)^2 + \int_0^{2\pi} A'(r,\lambda,z,t)^2 d\lambda/2\pi}, \tag{1}$$

where A is a physical variable (e.g., tangential wind, vorticity and PV); r and λ are the radial and tangential direction, respectively; and the prime stands for the deviation from the azimuthal average. In this study, tangential wind is used as A in Eq. (1). Figures

5b and 5c show increases in mid-level PV, inertial stability above 4-km height and axisymmetricity throughout the troposphere about 4-6 h prior to RI, consistent with Rogers (2010) and Miyamoto and Takemi (2013), which suggested that the increased PV and the axisymmetric vortex structure would be a good indicator of whether a TC is undergoing RI. Unlike the axisymmetric dynamical structure shown in Fig. 5b, the convective pattern prior to the RI is asymmetric and becomes more symmetric 3 h after the RI commences (Fig. 6), suggesting that the axisymmetric convective ring may be the result instead of the cause for RI in this case. The asymmetric convective pattern prior to RI is rather inconsistent with the observational findings (e.g., Kieper and Jiang 2012).

d. Evolution of the warm-core structure

A warm core with magnitude of 6-6.5 K located at z = 6 – 8 km is identified in Fig. 7a. The hydrostatic equation is used to assess the impact of this warm core on the reduction of MSLP. Figure 7b indicates that the diagnostic pressure is about 3-4-hPa higher than the modeled pressure. It is speculated that this error may be ascribed to the rather insufficient vertical resolution, which can't resolve the comprehensive vertical virtual temperature distribution at the TC center. Nevertheless, the error would not affect the relative importance of this warm core. The warming above 5 km contributes more to the MSLP reduction (Fig. 7b). It is thus hypothesized that the warm core located at mid level may be one of the important precursors prior to RI. Furthermore, the mid-level warm core is stronger at the onset of RI than that 6 to 12 h prior to RI, suggesting that the warm core at z = 6 – 8 km with certain strength (about 6.5 K) is important for the onset of RI. The possible mechanisms contributing to the formation of the mid-level warm core are discussed in section 5.

It should be mentioned that the reference temperature profile used to calculate the warm-core anomaly is defined as the averaged virtual temperature within the 558-648-km annulus moving with the storm at the same time, same as the reference state used in Stern and Nolan (2012). In addition, the details regarding the calculation of hydrostatic pressure are shown in Appendix F.

e. Convective-scale evolution

Several periods with active convection composed of weak-to-moderate convection and CBs can be identified (Fig. 8a) prior to RI. Simultaneously, the latent heat increases significantly inside the RMW (Fig. 9c), where the heating could strengthen the warm core effectually (Vigh and Schubert 2009). Note that the active convection is located outside or around the low-level RMW (Figs. 8a and 1b), while it lies inside the mid-upper-level RMW (Figs. 8a), consistent with the findings in Susca-Lopata et al. (2015). Therefore, the latent heat mainly increases substantially within the mid-upper troposphere inside the RMW (Fig. 9c). The increased latent heat is mostly caused by the weak-to-moderate convection, while the CBs confined to tiny areas also play some nonnegligible role (Figs. 9a and 9b). From another viewpoint, during the periods with active convection, both the increased weak-to-moderate convection and CBs are located at inner radius with higher inertial stability (Figs. 8b and 8c), which is the only factor determining the heating efficiency in this study. Other parameters affecting Rossby deformation radius, such as static stability and scale height, almost do not change with time (figures not shown). It is believed that the active convection generating large amount of latent heat is indispensable to the strengthening of the vortex-scale secondary circulation. This hypothesis will be validated using a SE model in section 4. Meanwhile, comparing

Fig. 8 and Fig. 9 with Fig. 5, we note that during the periods with active convection, the total PV and mean inertial stability increase significantly, implying that the prosperous inner-core convection can facilitate the enhancement of TC dynamical structure. In addition, the dynamical axisymmetricity decreases strikingly before gradually increasing when vigorous convection begins to develop. It is speculated that the seesaw between the asymmetric – symmetric TC structures prior to 1300 UTC 15 October, congruent with the numerical results conducted by Nguyen et al. (2011) during the intensification of the simulated Hurricane Katrina (2005), appears to play an important role in transferring the kinetic energy from the eddies to the mean flows. The increased kinetic energy in the mean flow, indicating enough vortex-scale inertial stability, is essential to the onset of RI (e.g., Rogers 2010).

An interesting characteristic is that both the CBs and weak-to-moderate convection are relatively inactive during 1400 UTC to 1800 UTC 15 October (Fig. 8a). This period with silent convection may impede the onset of RI, thus delayed until 1800 UTC 15 October. Furthermore, it can be noted that the convection becomes more active with the moderate increase of the latent heat between 1800 to 2100 UTC 15 October (Figs. 8a and 9c), which could play a favorable role in the triggering/maintenance of RI.

4. More insights from the PV budget and Sawyer-Eliassen model

In the previous section, the temporary inner-core active convection, gradually strengthened primary circulation and a warm core with certain strength at mid level (6-8-km height) are identified prior to RI. It is of scientific interest to examine the physical relation between the active convection and the gradually improved storm structure. Namely, the aim is to find out how the active convection contributes to the increased PV, especially within the mid-upper troposphere (about 5-9-km altitude). Whether the convection in the inner-core region is active or inactive is defined by the criteria of 0.53% CB's areal percentage inside the radius of 80 km. Periods in which CB's areal ratio exceeds (less than) 0.53% are defined as "active CB phase" ("non-active CB phase"). The durations of these two phases are equally both 7.5 h prior to the onset of RI. Figure E1 shows the distributions of active CB phase and non-active CB phase. Note that the weak-to-moderate convection is also relatively more vigorous during the active CB phase (Fig. 8a), suggesting that the areal ratio of CBs is an ideal index for determining whether the inner-core convection is active or not. The first 3 h integration during the early spin-up period is excluded in our calculation. Figure 10a quantitatively demonstrates that the PV tendency above 5-km height during the active CB phase is substantially larger than that during the non-active CB phase. It is also worth pointing out that the PV tendency above 5-km height during the non-active CB phase is negative, suggesting that active convection provides necessary conditions for mid-upper-level PV to increase. The PV budget is conducted to clarify the processes contributing to the different PV tendencies (Figs. 10b, c, d) between the active and the non-active CB phases. The approximate PV tendency equation neglecting the frictional effect and the vorticity associated with the vertical velocity (e.g., Wu et al. 2016) in a height coordinate can be written as:

$$\frac{\partial P}{\partial t} = -\boldsymbol{V} \cdot \nabla_h P - w\frac{\partial P}{\partial z} + \rho^{-1}\nabla_3 \cdot (Q\boldsymbol{q}), \tag{2}$$

Eq. (2) is integrated over area of a circle with the radius of 80 km:

$$\int_{r_0}^{r_{80}}\int_0^{2\pi}\frac{\partial P}{\partial t}d\lambda\,\mathrm{dr} = -\int_{r_0}^{r_{80}}\int_0^{\boldsymbol{2\pi}}\boldsymbol{V} \cdot \nabla_h P\,\mathrm{d}\lambda\mathrm{dr} - \int_{r_0}^{r_{80}}\int_0^{2\pi} w\frac{\partial P}{\partial z}d\,\lambda dr +$$

$$\int_{r_0}^{r_{80}}\int_0^{2\pi}\rho^{-1}\nabla_3(Q\boldsymbol{q})\,\mathrm{d}\lambda\mathrm{dr}, \tag{3}$$

$$\mathrm{P} = \frac{1}{\rho}\left[(\xi + f)\frac{\partial\theta}{\partial z} - \frac{\partial v}{\partial z}\frac{\partial\theta}{\partial x} + \frac{\partial u}{\partial z}\frac{\partial\theta}{\partial y}\right], \tag{4}$$

where P is PV, $\boldsymbol{V}$ is horizontal wind**,** ∇_h the horizontal gradient operator, w vertical velocity, ρ density, Q diabatic heating rate, $\boldsymbol{q}$ the absolute vorticity vector**,** ξ the relative vorticity and ∇_3 the three-dimensional gradient operator. The net PV tendency is determined by three terms on the right-hand side of (2): the horizontal advection, the vertical advection and the diabatic heating (DH) terms that depend on gradients of Q and q. It is acceptable that the frictional effect is ignored in Eq. (3) (e.g., Wang 2014; Harnos and Nesbitt 2016b; Wu et al. 2016), since the increase of PV mainly concentrates above the boundary layer (Fig. 5b).

It should be known that the calculation of PV budget and the following SE model diagnoses are based on another experiment (CTRL_1min) with the same settings as CTRL, except that the temporal resolution of the output is increased to 1 min. In addition, the output vertical grid meshes are interpolated to 45 levels but the number of vertical levels for numerical integration is still 35 layers. On top of that, the 1-2-1 smoother has been applied to x, y and z directions for the PV tendency and three diagnostic terms on the right-hand side of Eq. (3).

For the levels above 5-km height, the increased PV tendency during active CB phase is mainly provided by the horizontal advection and vertical advection terms (Figs. 10b, c). Although the DH term offsets most of the positive PV tendency contributed by the advective terms (Fig. 10d), the sum of the three terms on the right-hand side of (2) is still positive above 5-km height. The horizontal advection term seem to contribute more PV tendency in the mid-upper levels (z = 4 – 8 km), and the vertical advection term provides more PV tendency in the upper levels (z > 8 km), while the DH term offsets a great amount of the increased PV caused by the vertical advection term in the upper levels. In general, the vertical advective effect redistributes the PV, namely transporting the PV from the lower troposphere to the mid-upper troposphere. The amplitudes of the advective PV tendencies including the horizontal and vertical PV advections are greater during the active CB phase, and it is speculated that this may be related to the different vortex structure and strength of secondary circulation between the active CB phase and the non-active CB phase. The mean properties of these fields are shown in Fig. 11.

The axisymmetric upper-level outflow, upward motions and diabatic heating are clearly greater during the active CB phase. In addition, the weak axisymmetric radial outflow within the radius of 30-40 km can be identified during the active CB phase, while it is far away ($r > 80$ km) from the TC center during the non-active CB phase. It is assumed that the stronger secondary circulation above the boundary layer is evoked by the larger latent heat associated with more vigorous convection during the active CB phase. In addition, the more intense primary circulation throughout the troposphere during the non-active CB phase appears to be a consequence of the stronger secondary circulation during the active CB phase, since the active CB phase precedes the non-active CB phase (Fig. E1). In the following analyses, the balanced model based on the SE equation (Eliassen 1951; Shapiro and Willoughby 1982; Hack and Schubert 1986) is employed to elucidate the relative relationship between the latent heat and the secondary circulation as well as the possible impact of different patterns of secondary circulation on the evolution of vortex structure. The details of the balanced model are depicted in Appendix D.

Figures 12a and 12b show axisymmetric tangential wind and diabatic heating at moments chosen from the active CB phase and the non-active CB phase, respectively.

It is clear that the latent heat during the active CB phase is much greater than that during the non-active CB phase, and that the balanced transverse circulation during the active CB phase is much more intense. In other words, stronger radial inflow, outflow and upward motions are identified during the active CB phase (figure not shown). Figures 12c and 12d indicate that the PV advection resulted from the balanced transverse circulation is significantly larger in the mid-upper levels during the active CB phase. In addition, we break down the larger PV advection into the radial and vertical components, suggesting that the vertical advection occupies a more important part in increasing the mid-upper-level PV at 1248 UTC 15 Oct (Figs. 12e and 12f). However, the positive horizontal PV advection identified above 5-km height (Figs. 10b and 12f) is somewhat counter-intuitive since there is no larger PV at outer radii transported toward the inner-core region. Instead, the mid-upper-level outflow associated with the active convection (Fig. 11a) tends to transport the larger inner-core PV away from the TC center. A further investigation indicates that the increased PV mainly arises from the enhancement of vorticity (Fig. G1a). Upward transport of vorticity is an important source for the increased mid-upper-level vorticity during the active CB phase (Fig. G1b). The CBs make a substantial contribution to the upward vorticity flux (>50%) between 5-8 km in the inner-core region (Fig. G1c), corresponding to the insightful finding in Wang (2014). It is thus suggested that the CBs, releasing less diabatic heating than the weak-to-moderate convection (Fig. 9), likely have an important impact on the amplification of mid-upper-level vortex.

Overall, the results from the PV budget and SE model underscore the key role of strong secondary circulation associated with large latent heat generated by the active convection, which has a vital influence on the improvement of TC structure prior to RI.

Furthermore, the increased CBs during the active CB phase play a key role in transporting the momentum upward and intensifying the TC circulation above 5-km height.

5. Sensitivity experiment's results

a. Convective-scale, vortex-scale and warm-core comparisons

A series of experiments is carried out to evaluate the uncertainty of intensification rate under different cloud microphysical schemes. One should note that the onset timing of intensification for each simulation is different. The experiment employing WSM3 as the cloud microphysical scheme (WSM3) has the slowest intensification rate (Table 3) compared with other experiments including CTRL. Therefore, WSM3 is chosen for a comprehensive comparison with CTRL to verify the importance of the several precursors leading to RI identified in sections 3 and 4. Both WSM3 and CTRL experiments show similar intensities and tracks in the early stages of the simulations, but RI occurs only in CTRL, not in WSM3. In addition, the synoptic environmental conditions are similar between these two simulations, except that the stronger upper-level divergence is identified in CTRL (figure not shown). However, it is unclear whether RI is caused by the larger upper-level outflow or by other processes, such as more active inner-core convection. Therefore, it is necessary to further explore the inner-core processes in CTRL and WSM3.

Figures 13b and 13d show that more latent heat inside the RMW prior to RI can be identified in CTRL, especially above the melting layer (~4-km height). The RMWs for both simulations are examined and it is found that the RMW is slightly larger in WSM3 in the mid-upper levels (figures not shown). This indicates that heating within the

RMW is more efficient in amplifying the CTRL vortex due to both the stronger primary circulation and smaller RMW relative to WSM3. Grid points of the CBs and weak-to-moderate convection inside the RMW are more numerous in CTRL than those in WSM3 (Figs. 13a and 13c). Examinations of the total latent heat inside the RMW contributed by different types of precipitation show that the increased latent heat inside the RMW in CTRL (Fig. 13b), especially within 6-12-km height, is mostly contributed by the more active weak-to-moderate convection (Fig. 14). The more active CBs play a minor role in providing the increased latent heat inside the RMW for CTRL (Fig. 14). Figure 14 suggests that the active weak-to-moderate convection inside the RMW seems to be more important than the CBs in triggering the RI of CTRL.

The convective activity is closely related to the strength of the storm-scale secondary circulation, as validated in section 4. Figure 15 shows the time-averaged radial winds and contour frequency distributions (CFDs) of vertical velocity in CTRL and WSM3. Figure 15e indicates that the updrafts in CTRL are stronger than those in WSM3 mainly at $z = 1 – 8$ km and $z = 14 – 18$ km. For the downdraft distributions, the downward motions in CTRL are also stronger than those in WSM3 at $z = 3$ km and at $z = 14 – 16$ km. These characteristics are consistent with several previous studies (e.g., McFarquhar et al. 2012; Chen and Zhang 2013; Wang and Wang 2014), suggesting the presence of intense vertical velocity at upper troposphere prior to the onset of RI. Figures 15c, 15d and 15f show that the radial outflow at $z = 16$ km in CTRL is considerably greater than WSM3, corresponding to the stronger updrafts in the upper troposphere. In addition, the radial inflow outside the radius of 60 km in CTRL is slightly stronger than that in WSM3 in the boundary layer (Fig. 15f), and the enhanced convergence can be identified in CTRL between the radii of 50-70 km (figure not shown).

Those features are also connected to the more intense updrafts in the lower troposphere documented in CTRL (Fig. 15e).

Enough strength of primary circulation and warming at mid-upper altitude may also be crucial for initiating RI, as suggested by the previous analyses. It is shown that the inner-core PV, inertial stability and dynamical axisymmetricity are greater in CTRL than those in WSM3 (Figs. 5b, 5c, 16a, 16c and 16d). Remarkable differences are identified 4 - 6 h prior to 1800 UTC 15 Oct, especially above 5-km height. A comparison of warm-core structures reveals the presence of greater warming above z = 6 km in CTRL (Figs. 7a and 16b). It is also found that WSM3 has fewer mid-upper-level PV, inertial stability, latent heat, warming and weaker secondary circulation by comparing it with the other sensitivity experiments (Figs. B1-B4). These comparisons again confirm the relative importance of the indicators including the temporary active convection inside the RMW, sufficient strength of primary circulation and warm core with certain magnitude at 6-8-km height prior to RI, as suggested by previous analyses.

b. Causes leading to different warm-core developments

As shown in Fig. 8b, the warming above 5-km height could efficiently induce the MSLP drop. Therefore, it is of scientific interest to investigate what mechanisms contribute to the greater mid-level (z = 6-8 km) warming in CTRL. By comparing Figs. 13a and 13c with Figs. 7a and 16b, it can be noted that more vigorous convection precedes the formation of the warm core located at the mid level in CTRL. It is possible that the stronger latent heat has an important impact on the warm-core development. Note that Ohno and Satoh (2015) employed a SE model to diagnose the balanced response to heating. Their results showed that heating-induced transverse circulation significantly contributed to the warm-core formation near the tropopause. Therefore, we also utilize the SE model to evaluate the impact of secondary circulation on the developments of warm cores. Figures 17a and 17b show the selected profiles at the same time (1248 UTC 15 October) of azimuthal-mean latent heat and tangential wind from CTRL and WSM3, individually. These moments, prior to the different developments of warm cores, will be diagnosed by the SE model to understand the θ tendency associated with the balanced transverse circulation. Figure 17c indicates that the secondary circulation triggered by the greater latent heat in CTRL is critical to the stronger θ tendency within the eye. Furthermore, the height of the maximum diagnosed θ tendency in CTRL is consistent with the simulated warm-core height. In addition, not surprisingly, the θ tendency is mostly contributed by vertical advection (figures not shown). Under the axisymmetric framework, vertical downward advection is the only term that can contribute to the warming in the eye, since horizontal inward advection brings the lower-θ air outside the eye into the eye region, which tends to reduce the θ within the eye.

However, Stern and Zhang (2013) indicated that the eddy radial θ advection accounted for the warming within the eye during the RI period in an idealized TC simulation. Hence, the contribution from eddies is examined through the θ budget:

$$\frac{\partial\bar{\theta}}{\partial t} = \frac{d\bar{\theta}}{dt} - \bar{u}\frac{\partial\bar{\theta}}{\partial r} - \frac{\partial\overline{u'\theta'}}{\partial r} - \frac{\overline{u'\theta'}}{r} - \bar{w}\frac{\partial\bar{\theta}}{\partial z} - \frac{\partial\overline{w'\theta'}}{\partial z}, \tag{5}$$

Eq. (5) is integrated over a circle with the radius of 20 km, the areal average of Eq. (5) can be written as:

$$\frac{1}{B}\int_{r_0}^{r_{20}}\int_0^{\boldsymbol{2\pi}}\frac{\partial\bar{\theta}}{\partial t}\mathrm{d}\lambda\mathrm{dr} = \frac{1}{B}\Big[\int_{r_0}^{r_{20}}\int_0^{\boldsymbol{2\pi}}\frac{\mathrm{d}\bar{\theta}}{\mathrm{dt}}\mathrm{d}\lambda\mathrm{dr} - \int_{r_0}^{r_{20}}\int_0^{\boldsymbol{2\pi}}\bar{\mathrm{u}}\frac{\partial\bar{\theta}}{\partial \mathrm{r}}\mathrm{d}\lambda\mathrm{dr} - \int_{r_0}^{r_{20}}\int_0^{\boldsymbol{2\pi}}\Big(\frac{\partial\overline{\mathrm{u}'\theta'}}{\partial \mathrm{r}} - \frac{\overline{\mathrm{u}'\theta'}}{\mathrm{r}}\Big)\mathrm{d}\lambda\mathrm{dr} - \int_{r_0}^{r_{20}}\int_0^{\boldsymbol{2\pi}}\bar{\mathrm{w}}\frac{\partial\bar{\theta}}{\partial \mathrm{z}}\mathrm{d}\lambda\mathrm{dr} - \int_{r_0}^{r_{20}}\int_0^{\boldsymbol{2\pi}}\frac{\partial\overline{\mathrm{w}'\theta'}}{\partial \mathrm{z}}\mathrm{d}\lambda\mathrm{dr}\Big], \tag{6}$$

where B equals to $\int_{r_0}^{r_{20}}\int_0^{\boldsymbol{2\pi}} \mathrm{d}\lambda \mathrm{dr}$, u is the radial wind, and the overbars denote the azimuthal mean. In addition, $\frac{\partial\bar{\theta}}{\partial t}$ is the azimuthal mean θ tendency, $\frac{d\bar{\theta}}{dt}$ is the diabatic heating term (DH), including the model-output latent heat and θ tendency due to effects of radiations and PBL parameterization, $-\bar{u}\frac{\partial\bar{\theta}}{\partial r}$ is the θ tendency due to azimuthal mean radial θ advection, and $-\frac{\partial\overline{u'\theta'}}{\partial r}-\frac{\overline{u'\theta'}}{r}$ is the θ tendency due to eddy component of radial θ advection (ERAD). On the vertical advection terms, $-\bar{w}\frac{\partial\bar{\theta}}{\partial z}$ is the θ tendency from azimuthal mean vertical θ advection (MVAD), and $-\frac{\partial\overline{w'\theta'}}{\partial z}$ represents the θ tendency caused by eddy component of vertical θ advection. These terms are calculated at 2-min intervals on the height coordinates. Figures 18c and 18d show each term of Eq. (6) averaged within the radius of 20 km at 1248 UTC 15 October, respectively. The contributions from azimuthal mean radial θ advection and eddy component of vertical θ advection to the warming can be basically neglected. It should be noted that the effect of diabatic heating is comparable with the advective terms, and CTRL features more warming due to diabatic heating at z = 8 – 10 km. This may be related to more stratiform precipitation moving into the eye at this moment (figure not shown), since CTRL has more vigorous convection inside the RMW. In addition, these analyses indicate that the warming caused by ERAD is as critical as the warming from MVAD (Fig. 18a), and that the asymmetric horizontal advection contributes greater warming at low troposphere in CTRL, as compared with WSM3 (Fig. 18c). Furthermore, the θ budgets at 0800 UTC 15 October, when the warm cores of CTRL and WSM3 newly formed, are also performed (Figs. 18a and 18b). Note that the incipient warm core at 7-km height in CTRL is stronger than that in WSM3 (Figs. 7a and

16b) at 0800 UTC 15 October. Figure 18a indicates that the azimuthal-mean subsidence plays an essential role in the greater warming above z = 6 km in CTRL, as compared with that in WSM3 (Fig. 18b). Despite that there are some residual errors in the lower troposphere in CTRL (Fig. 18a), this result demonstrates that the azimuthal-mean subsidence that may be related to the detrainment of active convection inside the RMW (Fig. 13a) is the critical mechanism leading to the formation of mid-level warm core in CTRL.

These results suggest that MVAD contributes to the formation of incipient mid-level warm core in CTRL, while ERAD also accounts for the low-level warming that can't be ignored in the eye. In addition, these mechanisms seem to be more active in rapidly intensifying TCs.

c. Understanding the factors affecting convective activities

The above results suggest that more vigorous convection generating greater latent heat inside the RMW is a key initial condition responsible for the onset of RI. Therefore, factors contributing to the active convection should be clarified. Rogers et al. (2013) proposed that the slope of eyewall convection, outer-core inertial stability in lower troposphere which would affect the strength of inflow and the radius of super-gradient wind may determine the radial distribution of upward motions, thus creating the difference of latent heat relative to the RMW. These possible factors are examined during 1100 UTC to 1300 UTC 15 October, when the convection in CTRL is significantly more vigorous than WSM3. However, the eyewall slope is more upright above z = 8 km in WSM3 than that in CTRL (Figs. 19a and 19b). Moreover, the difference of outer-core inertial stability is insignificant between CTRL and WSM3 and the radius of super-gradient wind is closer to the TC center in WSM3 than that in CTRL (figures not shown). Therefore, the difference of latent heat inside the RMW is resulted from the strength of convection, not from the location of it (Figs. 19a and 19b). Increased inner-core surface enthalpy flux (SEFX) is conducive to the eyewall active convection and TC intensity (Xu and Wang 2010). The SEFX is larger for most of the time during and prior to the development of active convection in CTRL than that in WSM3 (Fig. 19c). The magnitude of SEFX is associated with near-surface wind speed, and the surface radial inflow in CTRL is slightly more intense than that in WSM3 outside the radius of 60 km (Fig. 15f). We therefore suggest that the larger SEFX in CTRL may be mainly contributed by the stronger inner-core surface tangential wind. The azimuthal mean tangential wind in CTRL is roughly 3 - 6 m s^{-1} greater than that in WSM3, and this difference presents 2 h prior to the development of vigorous convection (figures not shown). The larger deficit of moisture near the surface may be another process contributing to the enhanced SEFX in CTRL. It is found that the moisture discrepancy between the oceanic surface and the lowest model level is larger in CTRL than that in WSM3 (figure not shown). The decreased moisture near the surface may be associated with the representation of graupel in WSM6 microphysics used in CTRL. The downdrafts caused by the fallout of graupel bring the cold and dry air to the surface layer, therefore the surface moisture decreases. The stronger downdrafts can also initiate convective cells, as suggested by Penny et al. (2016).

Recently, some researches proposed that eyewall intense convection could be triggered by the high-θ_e air transported from the eye (Barnes and Fuentes 2010; Miyamoto and Takemi 2013; Wang and Wang 2014), and this process may lead to RI. Figure 19d indicates that more high-θ_e air is transported into the eyewall in CTRL during the period with active convection. In addition, evaluation of the excess energy in the eye, as defined by Barnes and Fuentes (2010), shows that CTRL is characterized by less excess energy (figure not shown). This could be attributed to more high-θ_e air mixed into the eyewall in CTRL. However, from the energetic standpoint, this mechanism, compared with larger SEFX identified in CTRL, provides less fuel (J s^{-1}) for the development of convection. The energy coming from SEFX outside the radius of 30 km is at least two orders of magnitude larger than that provided by the transportation of high-entropy air from the eye to eyewall, consistent with the statement made by Bryan and Rotunno (2009). Consequently, the larger SEFX should be the dominant process leading to the active convection in CTRL.

6. Concluding remarks and discussions

This study aims to clarify the mechanisms leading to the RI of Typhoon Megi (2010). By comparing the best track, satellite and aircraft observational data, it is demonstrated that the RI process is reasonably well reproduced using a high-resolution WRF simulation. Furthermore, the PV budget and SE model are utilized to gain more physical insights between the different possible predecessors prior to RI. Finally, a series of sensitivity experiments is carried out to evaluate the validity of these precursors.

The results of PV budget show that when the CBs are active, the simulated PV tendency is remarkably greater above 5-km height. The increased CBs during the active CB phase, transporting a large amount of vorticity to the mid-upper levels, probably have a critical impact on the enhancement of vortex above 5-km height. In addition, the vertical advection makes an important contribution to the upper-level PV, and the intense updrafts may be triggered by the latent heat of active convection. The SE model is applied to diagnose the balanced response of latent heat and it is shown that when convection is vigorous, the enhanced latent heat strengthens the secondary circulation, which mainly enhances the vertical PV advection. The reinforced secondary circulation also contributes to the mid-level warming within the eye because it enhances the azimuthal mean subsidence, which is also the possible mechanism giving rise to the formation of mid-level warm core. On top of that, the results of θ budget indicate that the radial advection linked to eddy process plays a nonnegligible role in the warming at lower-level eye.

Comparisons of sensitivity experiments with different cloud microphysical schemes suggest that more active convection, particularly the larger areal coverage of weak-to-moderate convection, inside the RMW with greater latent heat, stronger secondary circulation, more robust primary circulation at mid-upper elevation and a mid-level warm core are the key indicators for RI. The larger SEFX accounts a major part in enhancing the more active convection in CTRL, while the transportation of high-θ_e air from the eye to eyewall is also helpful but to a much lesser amplitude than the former. In addition, the convective discrepancies between CTRL and WSM3 imply the potentially dominant role of the weak-to-moderate convection on the onset of RI, while the CBs play a supporting role yet to a lesser extent. Note that this relative importance is based on the modified partitioning algorithm given by Rogers (2010). The overall stronger convective strength (Fig. 15e and Fig. B4) is implicitly linked to the onset of RI since it is directly associated with the greater magnitude of vortex-scale secondary circulation above the boundary layer. Our study provides quantitative evidences (Fig. 15e and Fig. B4) in supporting the assumption by Rogers (2010) that the amplified secondary circulation has an essential role on the onset of RI and the critical role of weak-to-moderate convection, accordant with the observational findings documented by Tao and Jiang (2015). However, neither the gradually-increased trend nor the extremely large number of CBs seem to be an absolute necessity for RI.

On the other hand, our results suggest that the warming above 5-km height contributes to the MSLP drop efficiently, consistent with Chen and Zhang (2013). However, the simulated height of the warm core at the onset of RI is different from that in Chen and Zhang (2013), which showed that the upper-level warm core is located at z = 14 km. In our results, the warm core located at z = 6-8 km is more consistent with that in Stern and Nolan (2012) and Chen and Gopalakrishnan (2015), suggesting that the RI is not necessarily triggered by the upper-level warm core near the tropopause. Regarding the mechanisms contributing to the formation of the mid-level warm core, it is suggested that the azimuthal-mean subsidence associated with detrainment of active convection inside the RMW is the major process.,

On the vortex-scale evolutions, our results highlight the importance of strengthened primary circulation and increased dynamic axisymmetricity prior to the RI, which was documented in several previous studies (e.g., Rogers 2010; Miyomoto and Takemi 2013). Unlike the symmetric dynamic structure prior to RI, the convective pattern is more asymmetric due to the moderate-to-high VWS, similar to that in Chen and Gopalakrishnan (2015), which investigated the asymmetric RI of Hurricane Earl (2010). However, the convective evolution prior to the RI is somewhat inconsistent with the axisymmetric convective pattern observed by previous satellite-based studies (e.g., Kieper and Jiang 2012; Zagrodnik and Jiang 2014). These comparisons imply that the enhanced primary circulation and axisymmetric wind structure may be more important than the ring-like convective pattern in initiating RI.

Although many precursors responsible for RI found in this study (including the active convection inside the RMW, stronger secondary circulation, more mighty primary circulation and a warm core ascertained at mid altitude) are also identified by previous observational and numerical researches (e.g., Rogers et al 2013; Brown and Hakim 2014), our study highlights the role of the synergistic interactions between these characteristics in creating a favorable pre-RI condition. Namely, this research provides the possible physical links to bridge the gaps between the precursors leading to the RI proposed in previous studies. Our work is more comparable with Rogers (2010), which suggested that the changes of vortex structure play a key factor explaining why RI happens. Rogers (2010) proposed that the enhanced inertial stability and primary circulation, resulted from the amplified secondary circulation associated with increased convective precipitation, would be the essential signature prior to the RI. However, our result is somewhat different as compared to Chen and Zhang (2013) and Wang and Wang (2014), which highlighted that the RI onset is directly triggered by the upper-level warm core induced by the subsidence of stratospheric air. They father suggested that the subsidence with high-θ air is associated with the detrainment of CBs.

The discrepancies between CTRL and WSM3 also underscore that the ice processes play an important role in triggering/maintaining the RI, consistent with several previous studies (McFarquhar et al. 2012; Miller et al. 2015; Harnos and Nesbitt 2016b). The ice processes including graupel, supercooled water and sublimation are neglected in the microphysical treatment of WSM3. Therefore, the latent heat associated with ice processes is reduced in WSM3, as compared with CTRL using WSM6 as microphysical scheme.

As previously mentioned in section 2d, the convective-stratiform partitioning algorithm utilized in this study may underestimate the contributions from CBs. Several studies indicated CB's inherent vertical slope due to the slantwise convection within the eyewall (Wang 2014; Harnos and Nesbitt 2016b). Therefore, the actual contribution of latent heat provided by CBs would be probably greater than that shown in Fig. 9a if the vertical slope of CBs is considered. In contrast, the contribution from weak-to-moderate convection might be less than that identified in Fig. 9b since part of the weak-to-moderate convection could be the slantwise CBs.

In summary, a plausible path leading to RI is described in Fig. 20: gradually increased vortex-scale enthalpy flux plays a major role in leading to the development of temporal active convection. The accompanied reinforced secondary circulation results in the strengthened primary circulation at mid-upper level, which can also facilitate the formation of mid-level warm core. Additionally, the robust primary circulation at mid-upper troposphere protects the warm core from being disrupted by the ventilation effect, and the heating efficiency of the vortex enhances as well. The development of the warm core above 5-km height effectively lowers the MSLP. The strengthened inertial stability and the development of mid-level warm core provide a favorable environment for the onset of RI.

It is thus eager to know the applicability of the possible pathway leading to RI described in Fig. 20. We found that the relative humidity within the eye above 8-km height in CTRL is lower than that in WSM3 3-5 h prior to RI (figures not shown), suggesting that the onset of RI may be linked to the development of TC eye (Fig. 21). This is consistent with the previous numerical studies (e.g., Fig. 5e of Rogers 2010; Fig. 3a of Miller et al. 2015; Fig. 2a of Kanada and Wada 2015). However, the percentage of TCs having eyes prior to RI seems to be relatively low in reality. Observational studies indicated that the mean intensity of TC at the onset of RI is 58 kt in the North Atlantic (KD03), while the median intensity at which TC develops an eye is 56 kt (Vigh et al. 2012), implying that about half of TCs have eyes when the RI commences. Note that the simulated Megi's intensity exceeding 40 m s^{-1} (~78 kt) at the onset of RI is stronger than the observational mean value (Fig. 1a). Furthermore, Shu et al. (2012) indicated that around 37% of RI cases reach typhoon intensity (>62 kt) at the onsets of RI over the North Western Pacific. We therefore think the plausible route leading to RI may be applicable to around 30% of the rapidly-intensifying TCs over the North Western Pacific.

Further studies are needed to verify the path proposed above. The impact of different environmental flow on the predictability of RI also remains to be clarified. Studies with high-resolution ensemble simulations under different synoptic environment are worth being conducted to explore the impact of TC-environment interaction on storm intensity changes. In addition, more realistic partitioning algorithm considering the 3-D updraft-scale convection as in Wang (2014) or Harnos and Nesbitt (2016b) should be applied to future numerical studies. In the end, some spin-up signals may be mixed into the pre-RI characteristics in this study due to the poor representations of initial vortex-structure. Although those signals do not affect the robustness of the major findings in this study, suitable initialization schemes should be utilized in future works.

Acknowledgements:

This work is supported by the Ministry of Science and Technology of Taiwan under Grants MOST 104-2628-M-002-004, the Office of Naval Research through Grant ONR-N62909-13-1-NO73, and Microsoft Research Asia grant FY14-RES-SPONSOR-024. Valuable comments from three anonymous reviewers that helped improve the quality of the manuscript are highly appreciated.

Appendix A

List of Symbols and Abbreviations

TABLE A1 here

Appendix B

Verification of the precursors leading to RI in the other sensitivity experiments

We checked the inertial stability, PV, warm-core anomaly, radial inflow, column-accumulated total latent heat at different inertial stabilities and vertical velocity within the inner-core region for all the experiments (Fig. B1 to Fig. B4).

Basically, WSM3 has the weakest inertial stability at z = 4-7 km, the lowest PV at z = 6-11 km (Figs. B1), and the least warming within the eye above z = 6 km (Figs. B2). Furthermore, Fig. B3 indicates that WSM3 has the least latent heat within the grid points with inertial stability from 0.45×10^{-3} s^{-1} to 1×10^{-3} s^{-1}, which implies that WSM3 has the least latent heat at the mid-upper troposphere (z = 7-13 km). On top of that, the comparisons of radial wind and vertical velocity indicate that WSM3 has the weakest upper-level outflow and mid-upper-level updrafts (Fig. B4). Overall, these analyses demonstrate that WSM3 has the weakest primary circulation, secondary circulation, warm-core intensity and latent heat in the inner-core region prior to the onset of its intensification, as compared with other sensitivity experiments undergoing RI.

FIGURE B1 here

FIGURE B2 here

FIGURE B3 here

FIGURE B4 here

Appendix C

Experimental sigma coordinates

The 35 σ levels are given as follows: 1, 0.998, 0.993, 0.983, 0.970, 0.954, 0.934, 0.909, 0.880, 0.845, 0.807, 0.765, 0.719, 0.672, 0.622, 0.571, 0.520, 0.468, 0.420, 0.376, 0.335, 0.298, 0.263, 0.231, 0.202, 0.175, 0.150, 0.127, 0.106, 0.088, 0.070, 0.055, 0.040, 0.026 and 0.

Appendix D

The balanced model

Here we use the SE equation based on Hack and Schubert (1986) in height coordinates as given in Wu et al. (2016). The diagnostic equation for streamfunction is written as:

$$\frac{\partial}{\partial R}\left(q\frac{\partial R\varphi^*}{R\partial R}\right)+\frac{\partial}{\partial Z}\left(s\frac{\partial \varphi^*}{\partial Z}\right)=\frac{g}{\theta_0}\frac{\partial Q}{\partial R}, \tag{A1}$$

Where R, Z, θ_0 and Q each represents the potential radius {i.e., the radius at which a parcel must be moved (conserving angular momentum) in order to change its tangential velocity to zero}, height, potential temperature at surface, respectively; q is the static stability, which is equals to $\frac{\xi}{\rho f}\frac{g}{\theta_0}\frac{\partial\theta}{\partial Z}$; s is the inertial stability, which equals to $f^2\frac{R^4}{\rho r^4}$; u (the azimuthal mean radial wind is equal to $-\frac{1}{r\rho}\frac{\partial\varphi^*}{\partial Z}$); w (the azimuthal mean vertical wind is equal to $-\frac{1}{r\rho}\frac{\partial\varphi^*}{\partial r}$). In this study, the quantities used to define the vortex and its forcing in the SE model are directly derived from the WRF model simulation at 2-min intervals and converted into the cylindrical coordinates, and azimuthally averaged. The SE model is used to diagnose the axisymmetric secondary circulation and its accompanying PV advection with which the balanced vortex responds to the azimuthal averaged diabatic heating. Note that the SE boundary conditions are characterized by streamfunction values equal to zero. The equation is solved by numerical inversion, using the successive over relaxation scheme. In addition, the SE equation is solved with a radial grid spacing of 2 km (slightly larger than the horizontal resolution used in the simulation), while the vertical resolution is uniform with a grid spacing of 0.194 km extending from the surface to the 19.4-km height.

Appendix E

The distributions of the active CB phase and non-active CB phase

FIGURE E1 here

Appendix F

The calculation of hydrostatic pressure

The hydrostatic pressure is obtained by integrating the hydrostatic equation $\{P_{sur} = P_{top} e^{\int_{H_{sur}}^{H_{top}} \frac{g}{R_d T_v} dz}$, P_{sur} (H_{sur}) is the surface pressure (height), P_{top} (H_{top}) is the pressure (height) at model top, R_d is the dry-air constant (287 J K^{-1} kg^{-1}), and T_v is the virtual temperature at each level $(T_v(z,t) = T_v(z) + T_v'(z,t))\}$ from the surface upward to the model top. $T_v(z)$ is the virtual temperature at initial time, and $T_v'(z,t)$ considers warming of the entire column.

Appendix G

The implication of CB for vertical vorticity transport

FIGURE G1 here

References

Andrew B. Penny, Patrick A. Harr, and James D. Doyle, 2016: Sensitivity to the representation of microphysical processes in numerical simulations during tropical storm formation. *Mon. Wea. Rev.*, **144**, 3611-3630.

Barnes, G. M. and P. Fuentes, 2010: Eye Excess Energy and the Rapid Intensification of Hurricane Lili (2002). *Mon. Wea. Rev.*, **138**, 1446-1458.

Brown, B., and G. Hakim, 2015: Sensitivity of intensifying Atlantic hurricanes to vortex structure. *Q. J. R. Meteorol. Soc.*, **141**, 2538-2551.

Braun, S. A., 2002: A Cloud Resolving Simulation of Hurricane Bob (1991): Storm Structure and Eyewall buoyancy. *Mon. Wea. Rev.*, **130**, 1573-1592.

Bryan, G. H., and R. Rotunno, 2009: The Influence of Near-Surface, High-Entropy Air in Hurricane Eyes on Maximum Hurricane Intensity. *J. Atmos. Sci.*, **66**, 148-158.

Cangialosi, J. P., and J. L. Franklin, 2012a: Atlantic and eastern North Pacific forecast verification. *Proc. 66th Interdepartmental Hurricane Conf.*, Charleston, SC, OFCM.

Chen, H., and D.-L. Zhang, 2013: On the Rapid Intensification of Hurricane Wilma (2005). Part II: Convective Bursts and the Upper-Level Warm Core. *J. Atmos. Sci.*, **70**, 146-162.

________, and S. G. Gopalakrishnan, 2015: A Study on the Asymmetric Rapid Intensification of Hurricane Earl (2010) Using the HWRF System. *J. Atmos. Sci.*, **72**, 531-550.

Cram, T. A., J. Persing, M. T. Montgomery, and S. A. Braun, 2007: A Lagrangian Trajectory View on Transport and Mixing Processes Between the Eye, Eyewall, and Environment Using a High-Resolution Simulation of Hurricane Bonnie

(1998). *J. Atmos. Sci.*, **64**, 1835-1856.

D'Asaro, E. A., P. G. Black, L. R. Centurioni, Y.-T. Chang, S. S. Chen, R. C. Foster, H. C. Graber, P. Harr, V. Hormann, R.-C. Lien, I.-I. Lin, T. B. Sanford, T.-Y. Tang, and C.-C. Wu, 2013: Impacts of Typhoons on the Ocean in the Pacific: ITOP. *Bull. Amer. Meteor. Soc.*, **95**, 1405–1418.

DeMaria, M., C. R. Sampson, J. A. Knaff, and K. D. Musgrave, 2014: Is Tropical Cyclone Intensity Guidance Improving. *Bull. Amer. Meteor. Soc.*, **95**, 387–398.

Dudhia, J., 1989: Numerical Study of Convection Observed during the Winter Monsoon Experiment Using a Mesoscale Two-Dimensional Model. *J. Atmos. Sci.,* **46**, 3077-3107.

Eliassen, 1951: Slow thermally or frictionally controlled meridional circulation in a circular vortex. *Astrophys. Norv*, **5[2],** 19-60.

Elsberry, R. L., T. D. B. Lambert., and M. A. Boothe, 2007: Accuracy of Atlantic and Eastern North Pacific Tropical Cyclone Intensity Forecast Guidance. *Wea. Forecasting.*, **22**, 747-762.

Falvey, R., 2012: Summary of the 2011 Western Pacific/Indian Ocean tropical cyclone season. *Proc. 66th Interdepartmental Hurricane Conf.*, Charleston, SC, OFCM.

Fang, J., and F. Zhang, 2016: Contribution of tropical waves to the formation of Super Typhoon Megi (2010). *J. Atmos. Sci.*, in press.

Guimond, S. R., G. M. Heymsfield, and F. J. Turk, 2010: Multiscale Observations of Hurricane Dennis (2005): The Effects of Hot Towers on Rapid Intensification. *J. Atmos. Sci.,* **67**, 633-654.

Hack, J. J., and W. H. Schubert, 1986: Nonlinear response of atmospheric vortices to heating by organized cumulus convection. *J. Atmos. Sci.*, **43,** 1559-1573.

Harnos, D. S., and S. W. Nesbitt, 2011: Convective structure in rapidly intensifying cyclones as depicted by passive microwave measurements. *Geophys. Res. Lett.*, **38**, L07805.

________, and ________, 2016: Varied pathways for simulated tropical cyclone rapid intensification. Part II: Vertical motion and cloud populations. *Q. J. R. Meteorol. Soc.*, **142**, 1832-1846.

Hendricks, D. A., M. S. Peng, B. Fu, and T. Li, 2010: Quantifying Environmental Control on Tropical Cyclone Intensity Change. *Mon. Wea. Rev.*, **138**, 3243-3271.

Heymsfield, G. M., J. B., Halverson, J., Simpson, L., Tian, and T. P. Bui, 2001: ER-2 Doppler Radar Investigations of the Eyewall of Hurricane Bonnie during the Convection and Moisture Experiment-3. *Journal of Applied Meteorology J. Appl. Meteor.,* **40**, 1310-1330.

Hong, S.-Y., J. Dudhia, and S.-H. Chen, 2004: A revised approach to ice microphysical processes for the bulk parameterization of clouds and precipitation. *Mon. Wea. Rev.*, **132,** 103-120.

________, and J.-O. Lim, 2006: The WRF Single-Moment 6-class Microphysics Scheme (WSM6). *J. Korean. Meteor. Soc.*, **42**, 129-151.

________, N. Ying, and J. Dudhia, 2006: A New Vertical Diffusion Package with an Explicit Treatment of Entrainment Processes. *Mon. Wea. Rev.,* **134**, 2318-2341.

Kain, J., and J. Fritsch, 1993: Convective parameterization for mesoscale models: The Kain-Fritsch scheme. The Representation of Cumulus Convection in Numerical Models, *Meteor. Monogr.,* **24**, 165-170.

________, J., 2004: The Kain-Fritsch Convective Parameterization: An Update. *J. Appl. Meteor.,* **43**, 170-181.

Kanada, S., and A. Wada, 2015: Numerical Study on the Extremely Rapid Intensification of an Intense Tropical Cyclone: Typhoon Ida (1958). *J. Atmos. Sci.*, **72**, 4194-4217.

Kaplan, J., and M. DeMaria, 2003: Large-Scale Characteristics of Rapidly Intensifying Tropical Cyclones in the North Atlantic Basin. *Wea. Forecasting.*, **18**, 1093-1108.

Kaplan, J., M. DeMaria, and J. A. Knaff, 2010: A Revised Tropical Cyclone Rapid Intensification Index for the Atlantic and Eastern North Pacific Basins. *Wea. Forecasting.*, **25**, 220-241.

Kelley, O. A., J. Stout, and J. B. Halverson, 2005: Hurricane Intensification Detected by Continuously Monitoring Tall Precipitation in the Eyewall. *Geophys. Res. Lett.*, **32**, L20819.

Kieper, M., and H. Jiang, 2012: Predicting tropical cyclone rapid intensification using the 37 GHz ring pattern identified from passive microwave measurements. *Geophys. Res. Lett.*, **39**, L13804.

Knaff, J. A., C. R. Sampson, M. DeMaria, T. P. Marchok, J. M. Gross, and C. J. Mcadie, 2007: Statistical Tropical Cyclone Wind Radii Prediction Using Climatology and Persistence. *Wea. Forecasting.*, **22**, 781-791.

Li, X., and Z. Pu, 2008: Sensitivity of Numerical Simulation of Early Rapid Intensification of Hurricane Emily (2005) to Cloud Microphysical and Planetary Boundary Layer Parameterizations. *Mon. Wea. Rev.*, **136**, 4819-4838.

Marks, F. D., and L. K. Shay, 1998: Hurricane Isabel (2003): Landfalling tropical cyclones: Forecast problems and associated research opportunities. *Bull. Amer. Meteor. Soc.*, **79**, 305-323.

McFarquhar, G. M., B. F. Jewett., M. S. Gilmore., S. W. Nesbitt. and T.-L. Hsieh, 2012:

Vertical Velocity and Microphysical Distributions Related to Rapid Intensification in a Simulation of Hurricane Dennis (2005). *J. Atmos. Sci.,* **69**, 3515-3534.

Miller, W., H. Chen, and D. Zhang, 2015: On the Rapid Intensification of Hurricane Wilma (2005). Part III: Effects of Latent Heat of Fusion. *J. Atmos. Sci.,* **72**, 3829-3849.

Miyamoto, Y., and T. Takemi, 2013: A Transition Mechanism for the Spontaneous Axisymmetric Intensification of Tropical Cyclones. *J. Atmos. Sci.,* **70**, 112-129.

Mlawer, E. J., S. J. Taubman, P. D. Brown, M. J. Iacona, and S. A. Clough, 1997: Radiative transfer for inhomogeneous atmospheres: RRTM, a validated correlated-k model for the longwave. *J. Geophys. Res. Soc.*, **102D**, 16663-16682.

Molinari, J., and D. Vollaro, 2010: Rapid Intensification of a Sheared Tropical Strom. *Mon. Wea. Rev.,* **138**, 3869-3885.

Montgomery, M. T., M. M. Bell, S. D. Aberson, and M. L. Black, 2006: Hurricane Isabel (2003): New Insights into the Physics of Intense Storms. Pert I: Mean Vortex Structure and Maximum Intensity Estimates. *Bull. Amer. Meteor. Soc.,* **87**, 1335-1347.

Nguyen, L. T., and J. Molinari, 2012: Rapid Intensification of a Sheared, Fast-Moving Hurricane over the Gulf Stream. *Mon. Wea. Rev.,* **137**, 603-631.

Nguyen, M. C., M. J. Reeder, N. E. Davidson, R. K. Smith, and M. T. Montgomery, 2011: Inner-core vacillation cycles during the intensification of Hurricane Katrina. *Q. J. R. Meteorol. Soc.* **140**, 3361-3378.

Ooyama K., 1969: Numerical Simulation of the Life Cycle of Tropical Cyclones. *J. Atmos. Sci.,* **26**, 3-40.

________, 1982: Conceptual Evolution of the Theory and Modeling of the Tropical Cyclone. *J. Meteor. Soc. Japan.* **60**, 369-380.

Persing, J., and M. T. Montgomery, 2003: Hurricane Superintensity. *J. Atmos. Sci.,* **60**, 2349-2371.

Reasor, P. D., M. D. Eastin. And J. F. Gamache, 2009: Rapidly Intensifying Hurricane Guillermo (1997). Part I: Low-Wavenumber Structure and Evolution. *Mon. Wea. Rev.*, **137**, 603-631.

Rogers, E., T. Black, B. Ferrier, Y. Lin, D. Parrish, and G. DiMego, 2001: Changes to the NCEP Meso Eta analysis and forecast system: Increase in resolution, new cloud microphysics, modified precipitation assimilation, and modified 3DVAR analysis. *NWS Tech. Procedures Bull.* **488**, NOAA/ NWS.

Rogers, R. F., 2010: Convective-Scale Structure and Evolution during a High-Resolution Simulation of Tropical Cyclone Rapid Intensification. *J. Atmos. Sci.,* **67**, 44-70.

________, P. D. Reasor., and S. Lorsolo, 2013: Airborne Doppler Observations of the Inner-Core Structural Differences between Intensifying and Steady-State Tropical Cyclones. *Mon. Wea. Rev.,* **141**, 2970-2991.

________, P. D. Reasor., and J. A. Zhang, 2015: Multiscale Structure and Evolution of Hurricane Earl (2010) during Rapid Intensification. *Mon. Wea. Rev.,* **143**, 536-562.

Schubert, W. H., and J. J. Hack, 1982: Inertial Stability and Tropical Cyclone Development. *J. Atmos. Sci.,* **39**, 1687-1697.

Shapiro, L. J., and H. E. Willoughby, 1982: The Response of Balanced Hurricanes to Local Sources of Heat and Momentum. *J. Atmos. Sci.*, **39**, 378-394.

Shu, S., J. Ming, and P. Chi, 2012: Large-Scale Characteristics and Probability of Rapidly Intensifying Tropical Cyclones in the Western North Pacific Basin. *Wea. Forecasting.*, **27**, 411-423.

Skamarock, W. C., and Coauthors, 2008: A description of the advanced research WRF version 3, 1-113 pp.

Spencer, R. W.,R. E. Hood, F. J. LaFontaine, E.A. Smith, R. Platt, J. Galliano, V. L. Griffin, and E. Lobl, 1994: High-resolution imaging of rain systems with the advanced microwave precipitation radiometer. *J. Atmos. Oceanic Technol*., **11**, 849–857.

Steiner, M., R. A. House, and S. E. Yuter, 1995: Climatological characterization of three-dimensional storm structure from operational radar and rain gauge data. *J. Appl. Meteor.*, **34**, 1978-2007.

Stern, D. P., and D. S. Nolan, 2012: On the Height of the Warm Core in Tropical Cyclones. *J. Atmos. Sci*, **69**, 1657-1680.

________, and F. Zhang, 2013: How Does the Eye Warm? Part I: A Potential Temperature Budget Analysis of an Idealized Tropical Cyclone. *J. Atmos. Sci.*, **70**, 73-90.

Stevenson, S. N., K. L. Corbosiero, and J. Molinari, 2014: The Convective Evolution and Rapid Intensification of Hurricane Earl (2010). *Mon. Wea. Rev.*, **142**, 4364-4380.

Susca-Lopata, G., J. Zawislak, E. J. Zipser, and R. Rogers, 2015: The Role of Observed Environmental Conditions and Precipitation Evolution in the Rapid Intensification of Hurricane Earl (2010). *Mon. Wea. Rev.*, **143**, 2207-2223.

Tao, C., and H. Jiang, 2015: Distributions of shallow to very deep precipitation/convection in rapidly intensifying tropical cyclones. *J. Climate*, **28,** 8791-8824.

Vigh, J. L., and Schubert, W. H., 2009: Rapid Development of Tropical Cyclone Warm Core. *J. Atmos. Sci.*, **66**, 3335-3350.

________, J. A. Knaff, and W. H. Schubert, 2012: A Climatology of Hurricane Eye Formation. *Mon. Wea. Rev.*, **140**, 1405-1426.

Wang, H., and Y. Wang, 2014: A numerical study of Typhoon Megi (2010): Part I: Rapid Intensification. *Mon. Wea. Rev.*, **124**, 29-48.

Wang, Z., 2014: Characteristics of Convective Processes and Vertical Vorticity from the Tropical Wave to the Tropical Cyclone Stage in the High-resolution Numerical Model Simulations of Tropical Cyclone Fay (2008). *J. Atmos. Sci.*, **71**, 896-915.

________, 2014: Role of Cumulus Congestus in Tropical Cyclone Formation in a High-Resolution Numerical Model Simulation. *J. Atmos. Sci.*, **71**, 1681-1700.

Wang, Y., and C.-C. Wu, 2004: Current understanding of tropical cyclone structure and intensity changes-A review. *Meteor. Atmos. Phys.*, **87**, 257-278.

Wu, C.-C., S.-N. Wu, H.-H. Wei, S. F. Abarca, 2016: The Role of Convective Heating in Tropical Cyclone Eyewall Ring Evolution. *J. Atmos. Sci.* **73**, 319-330.

Xu, J., and Y. Wang, 2010: Sensitivity of Tropical Cyclone Inner-Core Size and Intensity to the Radial Distribution of Surface Entropy Flux. *J. Atmos. Sci.*, ***67***(6), 1831-1852.

Zagrodnik, J. P., and H. Jiang, 2014: Rainfall, Convection, and Latent Heating Distributions in Rapidly Intensifying Tropical Cyclones. *J. Atmos. Sci.*, **71**, 2789-2809.

Zhang, D.-L., and H. Chen, 2012: Importance of the upper-level warm core in the rapid intensification of a tropical cyclone. *Geophys. Res. Lett.*, **39**, L02806.

1102

Table captions

TABLE 1. List of the cloud microphysics sensitivity experiments and their physics options.

TABLE 2. The mean magnitudes of the different synoptic variables identified in the first 18-h simulation in this study for the CTRL experiment and the statistical studies conducted by Kaplan and DeMaria (2003) and Kaplan et al. (2010). The REFC is the 200-hPa relative eddy flux convergence (m s^{-1} day^{-1}) averaged from r = 100-600 km, SST (°C) at the TC center, RHLO the 850-700-hpa mean relative humidity (%) averaged from r = 200-800 km, D200 the 200-hpa divergence (s^{-1}) averaged from r = 200-800 km, SHR the 850-200-hPa vertical shear(m s^{-1}) averaged from r = 200-800 km, and U200 the 200-hPa u (m s^{-1}) component of wind averaged from r = 200-800 km.

TABLE 3. List of the first 24-h intensification rates for different sensitivity experiments listed in Table. 1. Note that the onset times of intensification for each experiment are different.

TABLE A1. List of Symbols and Abbreviations. Table A1 provides a complete list of symbol and abbreviation definitions. Note that WSM3 not only indicates a specific microphysics scheme but also represents the experiment employing WSM3 as the microphysics scheme.

Figure captions

Figure 1. (a) The time series of WRF-forecasted maximum surface wind (m s^{-1}, red and black solid lines) and minimum central pressure (hPa, red line) from 0000 UTC 15 Oct to 0000 UTC 18 Oct 2010 based on the 6-h JTWC best track data (black dashed lines). (b) The time series of WRF-forecasted RMW (km, red and black solid lines) at z=0.02 km and observed RMW (black dashed line) from the 6-h JTWC best track data for the same period as Fig. 1a. The vertical black lines indicate the RI onset. The red lines are derived from the 10-min simulated results, and black solid lines are averaged within 1 h.

Figure 2. The WRF-forecasted track (blue line) and observed track (red line) from the JTWC best track data at 6-h intervals indicated by solid circles from 0000 UTC 15 Oct to 1800 UTC 18 Oct 2010. The model domains with triply nested, movable meshes (D02 and D03) used for the simulation are represented by the black rectangles.

Figure 3. (a) Column-integrated graupel mass content (g m^{-2}) derived from simulated fields with 1.33-km resolution at 2000 UTC 15 Oct. (b) 85-Ghz brightness temperature measured by Multifunctional Transport Satellite (MTSAT) at 1959 UTC 15 Oct. (c) Same as in Fig. 3a, but is for 0840 UTC 17 Oct. (d) Same as in Fig. 3b, but is for 0836 UTC 17 Oct. Note that the units of x and y-coordinates for (a) and (c) indicate the distance (km) from the TC center.

Figure 4. Flight-level winds (knot, red line), surface winds (knot, black line) for

radial through (a) simulated Megi at 1200 UTC 17 Oct, (b) simulated Megi at 2200 UTC 17 Oct, (c) Typhoon Megi observation from ITOP field program (0630, pass l). Solid blue dots represent the lowest 150-m dropsonde winds and the green line indicates the surface rain rate (mm h^{-1}). Fig. 4c comes from D'Asaro et al. (2013). The x-coordinates for Figs. 4a and 4b indicate distance (km) from the simulated TC center. The azimuthal angles of the radial profiles relative to the storm centers for Fig. 4a and 4b are similar to Fig. 4c.

Figure 5. (a) The radius-time cross section of the azimuthal mean for tangential wind (shaded, m s^{-1}) and radial wind (dashed contours at -3 intervals) at 0.02-km height. The azimuthal mean for vertical velocity at 2-km height is presented by thick black contours at 0.5-m s^{-1} intervals. (b) The time-height cross section of total PV (contour, PVU) and mean inertial stability (shaded, 10^{-4} s^{-1}) within a radius of 80 km from the simulated TC center. (c) The time-height cross section of the axisymmetricity associated with tangential wind within a radius from 20 to 80 km from the simulated TC center. (shaded, %). The black solid lines denote the onset of RI at 1800 UTC 15 Oct.

Figure 6. The time-azimuthal angle ($^\circ$) cross section of averaged simulated reflectivity (shaded, dBZ) within the radius of 20 and 80 km from the simulated TC center at 1-km height. The black line denotes the onset of RI.

Figure 7. (a) The time-height cross section of averaged Tv (K, contour) and Tv perturbation (K, shaded) within a radius of 20 km from the simulated TC center. (b) The time series of averaged surface pressure (hPa) within a radius of 20 km

from the simulated TC center of the model-output result (black line). The red line denotes the diagnostic pressure. The blue line denotes the diagnostic pressure from the Tv profile not considering the warming below 5.5-km height ($T_v'(z,t)$ below z=5.5 km equals to zero). The purple line denotes the diagnostic pressure from the temperature profile not considering the warming between 5.5-km and 11-km height ($T_v'(z,t)$ between z=5.5-11 km equals to zero). The black lines denote the onset of RI.

Figure 8. (a) The time-radius cross section of areal percentage accounted as weak-to-moderate convection (shaded, %) and CBs (red contour, at 5% interval) at different radius, overlaid with the RMW (black dots) at 7.5-km height. (b) The time-height cross section of averaged inertial stability (shaded, 10^{-4} s^{-1}) for grid points accounted as CBs within a radius of 80 km from the simulated TC center. (c) Same as in Fig. 8b, but is for weak-to-moderate convection.

Figure 9. (a) The time-height cross section of the total latent heat (10^4 K hr^{-1}) contributed by CBs within the RMW. (b) Same as in Fig. 9a, but is for weak-to-moderate convection. (c) The time-height cross section of the total latent heat within the RMW.

Figure 10. The height-potential vorticity tendency cross sections of (a) total PV tendency (PVU hr^{-1}) within a radius of 80 km from the simulated TC center. (b) Same as in Fig. 10a, but is for horizontal PV advection (10^3 PVU hr^{-1}). (c) Same as in Fig. 10a, but is for vertical PV advection (10^3 PVU hr^{-1}). (d) Same

as in Fig. 10a, but is for heating induced PV (10^3 PVU hr^{-1}). Black lines denote the active CB phase. Blue lines denote the non-active CB phase.

Figure 11. (a) The height-radius cross sections of time-averaged azimuthal mean radial wind (shaded, m s^{-1}) and vertical velocity (contours at 0.2–m s^{-1} intervals) during active CB phase. (b) Same as in Fig. 11a, but is for non-active CB phase. (c) The height-radius cross sections of time-averaged azimuthal mean latent heat (shaded, K hr^{-1}) and tangential wind (contours at 3–m s^{-1} intervals) during active CB phase. (d) Same as in Fig. 11c, but is for non-active CB phase.

Figure 12. (a) The height-radius cross section of azimuthal mean latent heat (shaded, K hr^{-1}) and tangential wind (contours at 4-m s^{-1} intervals) at 1248 UTC 15 Oct, one moment of active CB phase. (b) Same as in Fig. 12a, but is for 1508 UTC 15 Oct, one moment of non-active CB phase. (c) The height-radius cross section of PV advection (shaded, PVU hr^{-1}) due to the transverse circulation diagnosed by the SE model at 1248 UTC 15 Oct. (d) Same as in Fig. 12c, but is for 1508 UTC 15 Oct. (e) The height-radius cross section of PV advection (shaded, PVU hr^{-1}) due to the radial velocity diagnosed by the SE model at 1248 UTC 15 Oct. (f) Same as in Fig. 12e, but is for vertical velocity.

Figure 13. (a) Time series of the number of CB grid points (gray) within the RMW at 8-km height and the number of weak-to-moderate convection grid points (black) within the RMW at 3.35-km height for the CTRL experiment. (b) The time-height cross section of total latent heat (10^4 K hr^{-1}) within the RMW at

different levels for the CTRL experiment. (c) Same as in Fig. 13a, but is for the WSM3 experiment. (d) Same as in Fig. 14b, but is for the WSM3 experiment. The thick black lines denote the onset of RI in the CTRL experiment.

Figure 14. The time-averaged total latent heat inside the RMW (10^4 K hr^{-1}) contributed by different types of precipitation separated by the partitioning algorithm from Rogers (2010) for (a) CTRL and (b) WSM3 from 0300 UTC to 1800 UTC 15 October. The black lines denote the time-averaged total latent heat inside the RMW; the red lines the total latent heat contributed by CBs; the orange lines the total latent heat contributed by weak-to-moderate convection; the blue lines the total latent heat contributed by stratiform precipitation; the green lines the total latent heat contributed by other precipitation; and the purple lines the total latent heat contributed by no rain region.

Figure 15. (a) The time-averaged CFDs of simulated vertical velocity (m s^{-1}) at each height between 0300 UTC and 1800 UTC 15 Oct for the CTRL experiment; contours represent frequencies (%) of the occurrence of vertical velocity within a radius of 80 km from the simulated TC center. (b) Same as in Fig. 14a, but is for the WSM3 experiment. (c) The radius-height cross section of time-averaged azimuthal mean radial wind (m s^{-1}) between 0300 UTC and 1800 UTC 15 Oct for the CTRL experiment. (d) Same as in Fig. 14c, but is for WSM3 experiment. (e) Difference of frequencies (%) plotted is the

CFDs of vertical velocity for the CTRL experiment minus that for the WSM3 experiment. (f) Difference of wind speed (m s^{-1}) plotted is the azimuthal mean radial wind for the CTRL experiment minus that for the WSM3 experiment.

Figure 16. (a) The time-height cross section of total PV (10^4 PVU) within a radius of 80 km from the simulated TC center for the WSM3 experiment. (b) The time-height cross section of averaged θ (K, contour) and θ perturbation (K, shaded) within a radius of 20 km from the simulated TC center for the WSM3 experiment. The reference temperature profile is defined as the 960 km $\times$ 960 km area-averaged $\theta(z)$ centered at storm center at the initial time. (c) Same as in Fig. 15a, but is for mean inertial stability (10^{-4} s^{-1}). (d) The time-height cross section of mean axisymmerticity (%) within a radius between 20 and 80 km from the simulated TC center for the WSM3 experiment. The black lines denote the onset of RI in CTRL.

Figure 17. (a) Same as in Fig. 12a. (b) Same as in Fig. 12b, but is for the WSM3 experiment. (c) The total θ advection (contour, K hr^{-1}) due to the transverse circulation diagnosed by the SE model at 1248 UTC 15 Oct for the CTRL experiment (black line) and the WSM3 experiment (blue line) within a radius of 20 km from the simulated TC center.

Figure 18. Each term in Eq. (6) for (a) CTRL experiment and (b) WSM3 experiment at 0800 UTC 15 Oct. The black lines indicate azimuthal mean θ

tendency, the red lines the diabatic heating term (DH), yellow lines the θ tendency due to azimuthal mean radial θ advection**,** light-blue lines the θ tendency due to the eddy component of radial θ advection (ERAD), orange lines the θ tendency from azimuthal mean vertical θ advection (MVAD), and blue lines the θ tendency caused by the eddy component of vertical θ advection. These terms are calculated at 2 min intervals on the height coordinates. (c) Same as in Fig. 17a, but is at 1248 UTC 15 Oct. (d) Same as in Fig. 17b, but is at 1248 UTC 15 Oct.

Figure 19. (a) The height-radius cross section of time-averaged azimuthal mean latent heat (shaded, K hr^{-1}) and vertical velocity (contours at 0.2-m s^{-1} intervals) during 1100 UTC and 1300 UTC 15 Oct for the CTRL experiment. (b) Same as in Fig. 19a, but is for the WSM3 experiment. (c) The time series of mean enthalpy fluxes (J m^2) within a radius of 80 km from the simulated TC center for the CTRL (blue line) and WSM3 (red line) experiments. (d) The time series of mean radial θe fluxes (K hr^{-1}) from the eye to eyewall at the radius of 30 km below 1-km height for the CTRL (blue line) and WSM3 (red line) experiments.

Figure 20. Schematics of radial distributions of inner-core convection, latent heat, primary circulation, secondary circulation, transportation of high-θ_e from the eye to eyewall, azimuthal mean subsidence, surface enthalpy flux and warm-core structure in (a) CTRL and (b) WSM3. CTRL has several distinct features

prior to RI: more robust primary circulation and a warm core located at mid-upper level, resulted from the stronger secondary circulation. The more active convection with larger latent heat triggers the stronger secondary circulation. The larger surface enthalpy flux and barotropic-instability-induced transport of high-θe air from the eye to eyewall can be beneficial to the development of active inner-core convection.

Figure B 1. (a) The time-averaged area-mean inertial stability (10^{-4} s^{-1}) within a radius of 80 km averaged from 3 h prior to RI onset to RI onset for CTRL and other sensitivity experiments. (b) Same as in (a), but is for total potential vorticity (10^4 PVU). The blue lines are CTRL, red lines Kessler, green lines Lin, purple lines WSM3, cyan lines WSM5, orange lines Ferr, grey lines WDM5 and aqua lines WDM6. Note that the onset times of intensification for each experiment are different, and WSM3 failed to undergo RI during the first 24 h of intensification.

Figure B 2. (a) The time-averaged area-mean θ perturbation (K) within a radius of 20 km averaged from 3 h prior to RI onset to RI onset for CTRL and other sensitivity experiments. The blue lines are CTRL, red lines Kessler, green lines Lin, purple lines WSM3, cyan lines WSM5, orange lines Ferr, grey lines WDM5 and aqua lines WDM6. Note that the onset times of intensification for each experiment are different, and WSM3 failed to undergo RI during the first 24 h of intensification.

Figure B 3. (a) The time-averaged column-integrated total latent heat (K/hr) at different inertial stability values (10^{-3} s^{-1}) within a radius of 80 km averaged from 12 h prior to RI onset to RI onset for CTRL and other sensitivity experiments. The blue lines are CTRL, red lines Kessler, green lines Lin, purple lines WSM3, cyan lines WSM5, orange lines Ferr, grey lines WDM5 and aqua lines WDM6. Note that the onset times of intensification for each experiment are different, and WSM3 failed to undergo RI during the first 24 h of intensification.

Figure B 4. (a) The time-averaged area-mean radial wind (m s^{-1}) within the radius between 30 to 100 km averaged from 12 h prior to RI onset to RI onset for CTRL and other sensitivity experiments. (b) Same as in (a), but is for vertical velocity averaged within a radius of 80 km. The blue lines are CTRL, red lines Kessler, green lines Lin, purple lines WSM3, cyan lines WSM5, orange lines Ferr, grey lines WDM5 and aqua lines WDM6. Note that the onset times of intensification for each experiment are different, and WSM3 failed to undergo RI during the first 24 h of intensification.

Figure E 1. Time series from 0000 UTC to 1800 UTC 15 October of the areal percentage (%) of CBs inside the radius of 80 km from the simulated center. The red line denotes 1 % of CB's areal ratio, and the black line denotes the onset of RI. The moments in red shadow are defined as "active CB phase", and the moments in green shadow are defined as "non-active CB phase".

Figure G 1. The height-vorticity tendency cross sections of (a) total vorticity tendency (s^{-1} hr^{-1}) within a radius of 80 km. (b) Same as in Fig. R3-6a, but is for total vertical vorticity advection. (c) Total vertical vorticity advection (s^{-1} hr^{-1})

contributed by the CBs inside a radius of 80 km. Black lines denote the active CB phase. Blue lines denote the non-active CB phase.

TABLE 1. List of the cloud microphysics sensitivity experiments and their physics options.

Expt	Cloud Microphysics Option
KS	Kessler warm-rain scheme
Lin	Purdue Lin scheme
WSM3	WSM three-class simple ice scheme
WSM5	WSM five-class mixed-phase scheme
Ferr	Eta Ferrier scheme
WDM5	Version of WSM5 that is double-moment for warm-rain processes
WDM6	Version of WSM6 that is double-moment for warm-rain processes

TABLE 2. The mean magnitudes of the different synoptic variables identified in the 15-h simulation prior to RI in this study for the CTRL experiment and the statistical studies conducted by Kaplan and DeMaria (2003) and Kaplan et al. (2010). REFC is the 200-hPa relative eddy flux convergence (m s-1 day-1) averaged from r = 100-600 km, SST (°C) at the TC center, while RHLO is the 850-700-hpa mean relative humidity (%) averaged from r = 200-800 km, D200 the 200-hpa divergence (s-1) averaged from r = 200-800 km, SHR the 850-200-hPa vertical shear(m s-1) averaged from r = 200-800 km, and U200 the 200-hPa u (m s-1) component of wind averaged from r = 200-800 km.

Variable	Units	Simulated Mean	KD03 and K010 (RI)	KD03 and K010 (Non-RI)
REFC	m s^{-1} day^{-1}	0.34	0.9	2.4
SST	°C	30.1	28	28
RHLO	%	79.4	70	65
D200	10^{-6} s^{-1}	6.1	4.9	2.6
SHR	m s^{-1}	8.8	4.9	8.5
U200	m s^{-1}	2.4	-0.6	3.8

TABLE 3. List of the first 24-h intensification rates for different sensitivity experiments listed in Table. 1. Note that the onset times of intensification for each experiment are different.

Expt	Intensification Rate (10-Wind Speed)	Intensification Rate (MSLP)
CTRL	19 m s^{-1}	−35 hPa
KS	22 m s^{-1}	−39 hPa
Lin	24 m s^{-1}	−44 hPa
WSM3	13 m s^{-1}	−18 hPa
WSM5	23 m s^{-1}	−42 hPa
Ferr	19 m s^{-1}	−35 hPa
WDM5	16 m s^{-1}	−35 hPa
WDM6	16 m s^{-1}	−36 hPa

TABLE A1. List of Symbols and Abbreviations. Table A1 provides a complete list of symbol and abbreviation definitions. Note that WSM3 not only indicates a specific microphysics scheme but also represents the experiment employing WSM3 as the microphysics scheme.

Abbreviation	Definition
RI	rapid intensification
TC	tropical cyclone
PV	potential vorticity
KD03	Kaplan and DeMaria (2003)
VWS	vertical wind shear
CBs	convective bursts
RMW	the radius of maximum azimuthal mean wind
MSLP	minimum surface pressure
θ_e	equivalent potential temperature
θ	potential temperature
SCAPE	slantwise convective available potential energy
SE	Sawyer-Eliassen
JTWC	Joint Typhoon Warning Center
JMA	Japan Meteorological Agency
WSM6	the WRF single moment 6-class microphysics scheme
WSM3	the WRF single moment 3-class microphysics scheme
WSM3	the experiment employing WSM3 as the microphysics scheme
RRTM	Rapid Radiative Transfer Model
YSU	Yonsei University
CTRL	control simulation using WSM6 for microphysical scheme
REFC	relative eddy flux convergence
active CB phase	Periods in which CB's areal ratio exceeds 0.53 %
non-active CB phase	Periods in which CB's areal ratio less than 0.53 %
DH	diabatic heating terms in the PV and θ budget
CFDs	contour frequency distributions
ERAD	the θ tendency due to eddy component of radial θ advection
MVAD	the θ tendency from azimuthal mean vertical advection
SEFX	inner-core surface enthalpy flux
Tv	Virtual temperature

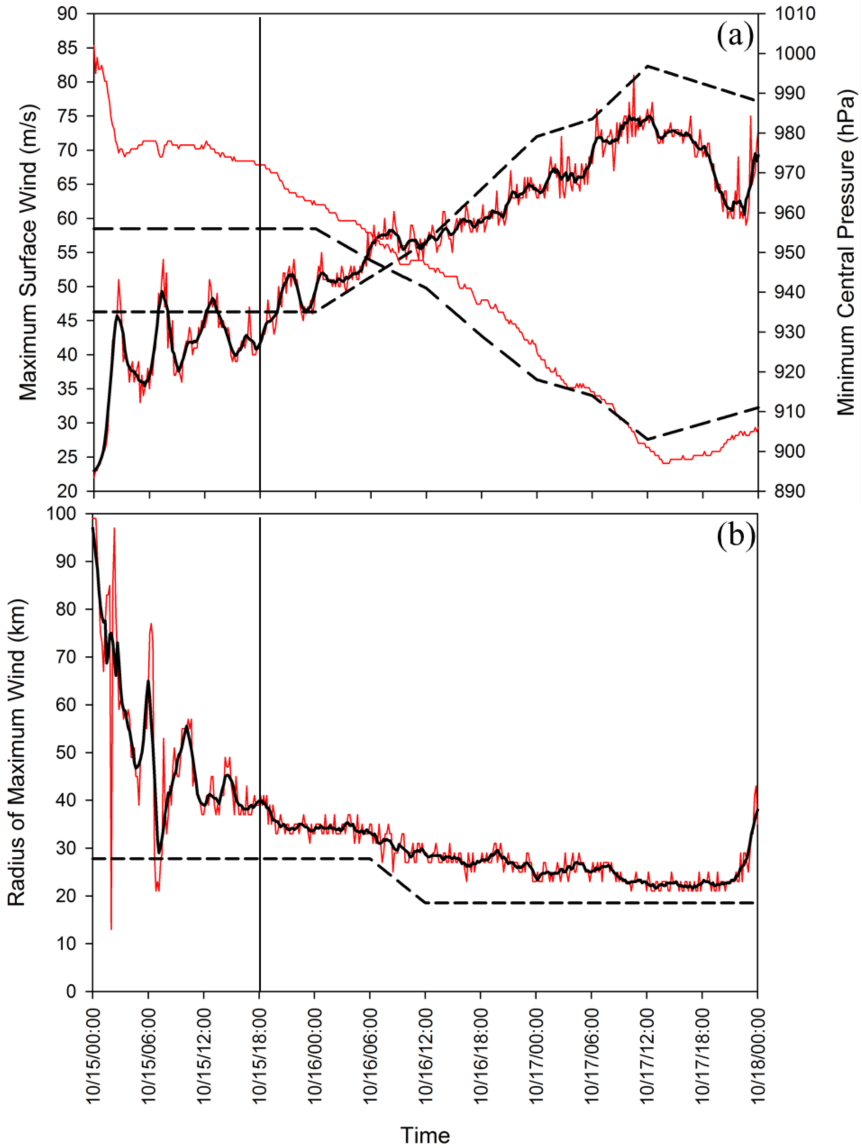

Figure 1. (a) The time series of WRF-forecasted maximum surface wind (m s^{-1}, red and black solid lines) and minimum central pressure (hPa, red line) from 0000 UTC 15 Oct to 0000 UTC 18 Oct 2010 based on the 6-h JTWC best track data (black dashed lines). (b) The time series of WRF-forecasted RMW (km, red and black solid lines) at z=0.02 km and observed RMW (black dashed line) from the 6-h JTWC best track data for the same period as Fig. 1a. The vertical black lines indicate the RI onset. The red lines are derived from the 10-min simulated results, and black solid lines are averaged within 1 h.

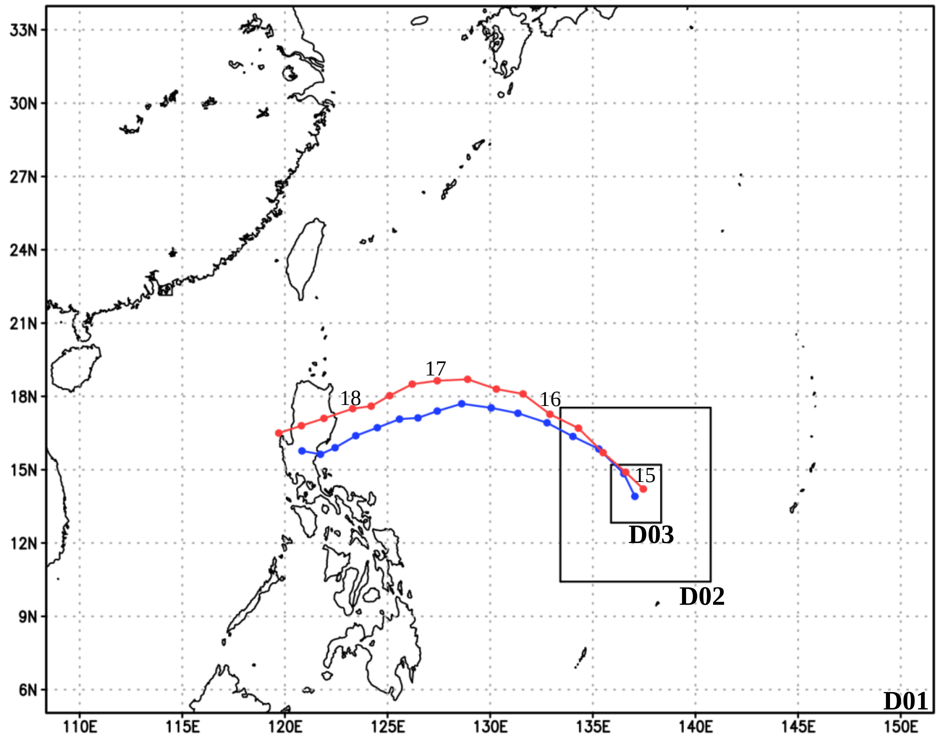

Figure 2. The WRF-forecasted track (blue line) and observed track (red line) from the JTWC best track data at 6-h intervals indicated by solid circles from 0000 UTC 15 Oct to 1800 UTC 18 Oct 2010. The model domains with triply nested, movable meshes (D02 and D03) used for the simulation are represented by the black rectangles.

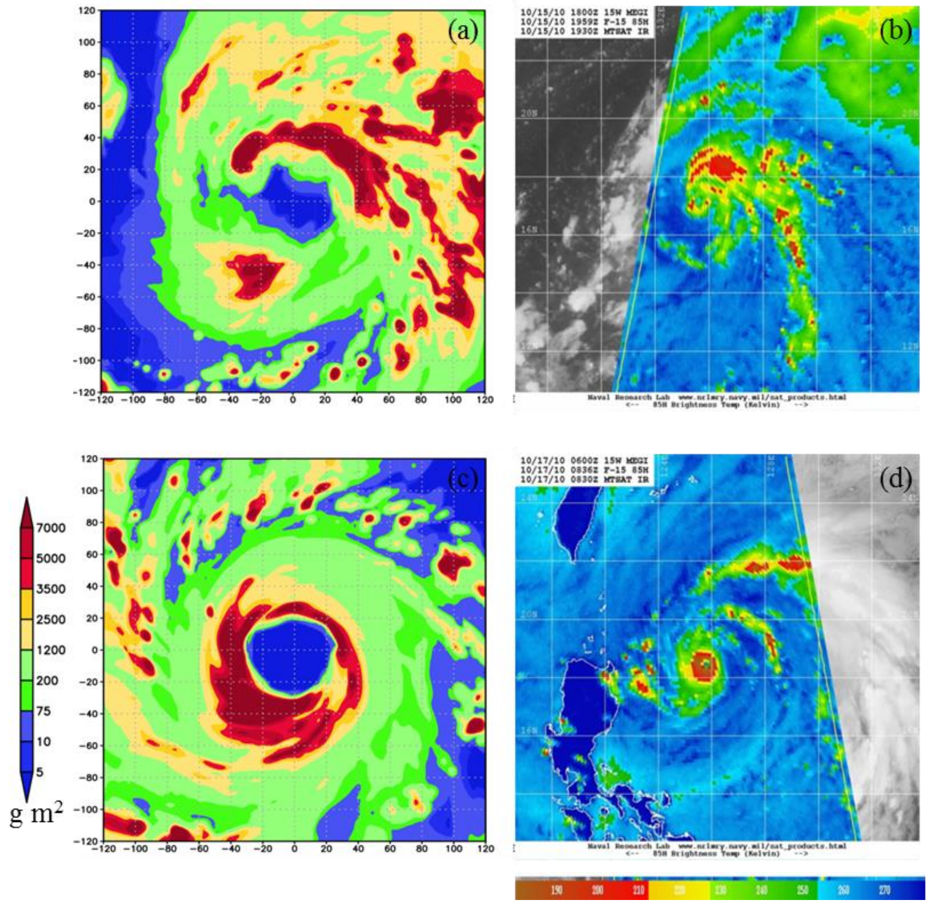

Figure 3. (a) Column-integrated graupel mass content (g m^{-2}) derived from simulated fields with 1.33-km resolution at 2000 UTC 15 Oct. (b) 85-Ghz brightness temperature measured by Multifunctional Transport Satellite (MTSAT) at 1959 UTC 15 Oct. (c) Same as in Fig. 3a, but is for 0840 UTC 17 Oct. (d) Same as in Fig. 3b, but is for 0836 UTC 17 Oct. Note that the units of x and y-coordinates for (a) and (c) indicate distance (km) from the TC center.

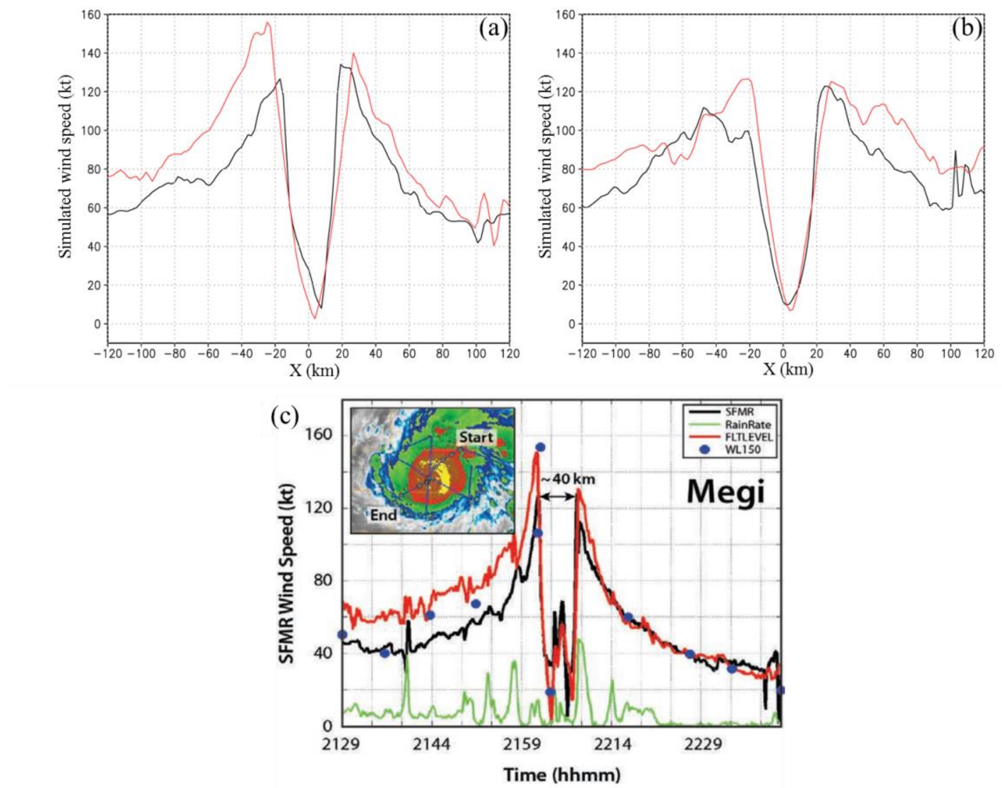

Figure 4. Flight-level winds (knot, red line), surface winds (knot, black line) for radial through (a) simulated Megi at 1200 UTC 17 Oct, (b) simulated Megi at 2200 UTC 17 Oct, (c) Typhoon Megi observation from ITOP field program (0630, pass l). Solid blue dots represent the lowest 150-m dropsonde winds and the green line indicates the surface rain rate (mm h^{-1}). Fig. 4c comes from D'Asaro et al. (2013). The x-coordinates for Figs. 4a and 4b indicate distance (km) from the simulated TC center. The azimuthal angles of the radial profiles relative to the storm centers for Fig. 4a and 4b are similar to Fig. 4c.

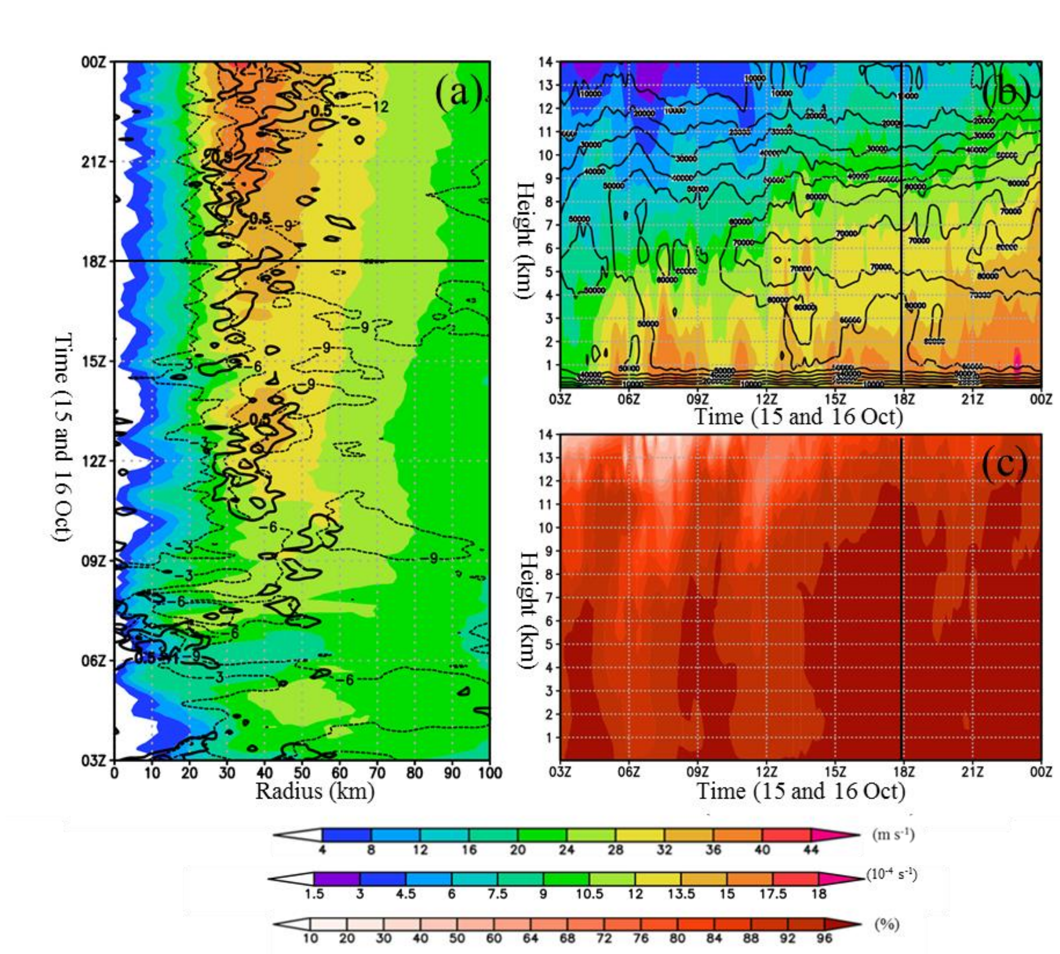

Figure 5. (a) The radius-time cross section of the azimuthal mean for tangential wind (shaded, m s^{-1}) and radial wind (dashed contours at -3 intervals) at 0.02-km height. The azimuthal mean for vertical velocity at 2-km height is presented by thick black contours at 0.5-m s^{-1} intervals. (b) The time-height cross section of total PV (contour, PVU) and mean inertial stability (shaded, 10^{-4} s^{-1}) within a radius of 80 km from the simulated TC center. (c) The time-height cross section of the axisymmetricity associated with tangential wind within a radius from 20 to 80 km from the simulated TC center (shaded, %). The black solid lines denote the onset of RI at 1800 UTC 15 Oct.

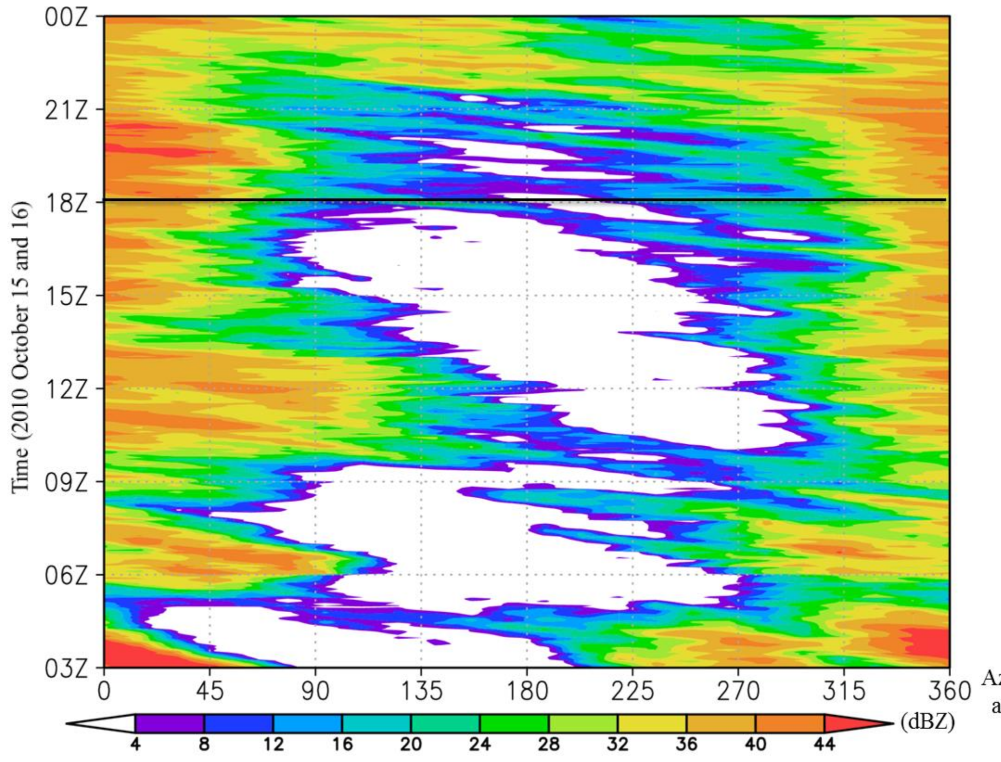

Figure 6. The time-azimuthal angle (°) cross section of averaged simulated reflectivity (shaded, dBZ) within the radius of 20 and 80 km from the simulated TC center at 1-km height. The black line denotes the onset of RI.

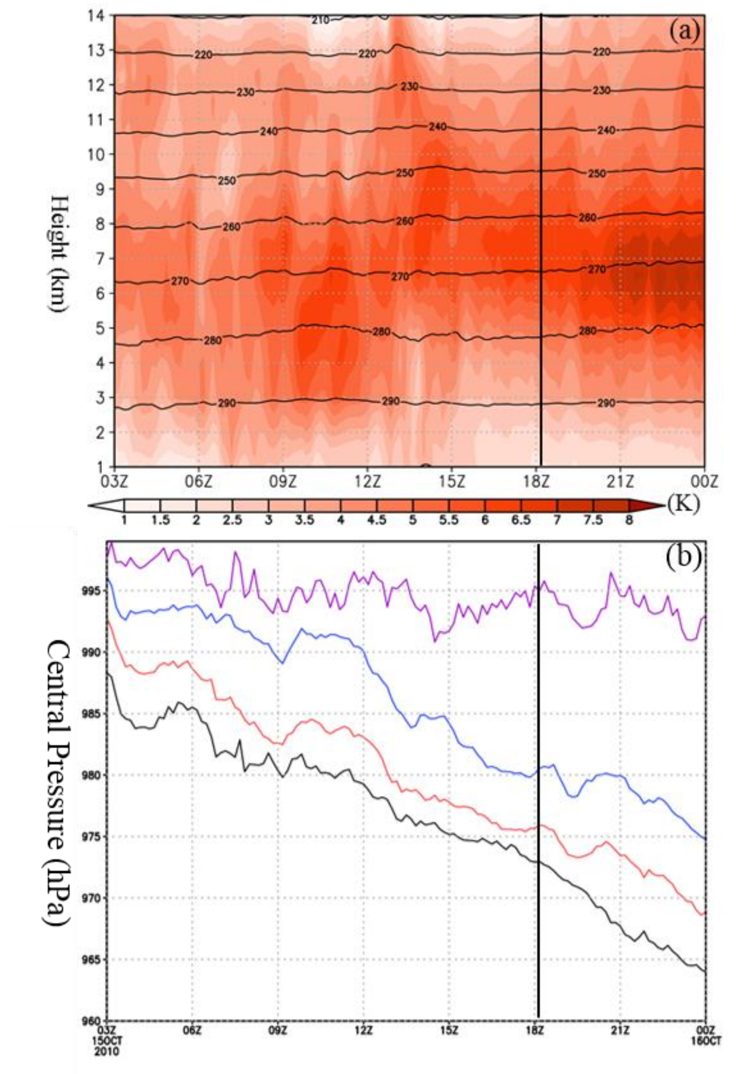

Figure 7. (a) The time-height cross section of averaged virtual temperature (Tv; K, contour) and Tv perturbation (K, shaded) within a radius of 20 km from the simulated TC center. (b) The time series of averaged surface pressure (hPa) within a radius of 20 km from the simulated TC center of the model-output result (black line). The red line denotes the diagnostic pressure. The blue line denotes the diagnostic pressure from the Tv profile not considering the warming below 5.5-km height ($T_v'(z,t)$ below z=5.5 km equals to zero). The purple line denotes the diagnostic pressure from the temperature profile not considering the warming between 5.5-km and 11-km height ($T_v'(z,t)$ between

z=5.5-11 km equals to zero). The black lines denote the onset of RI.

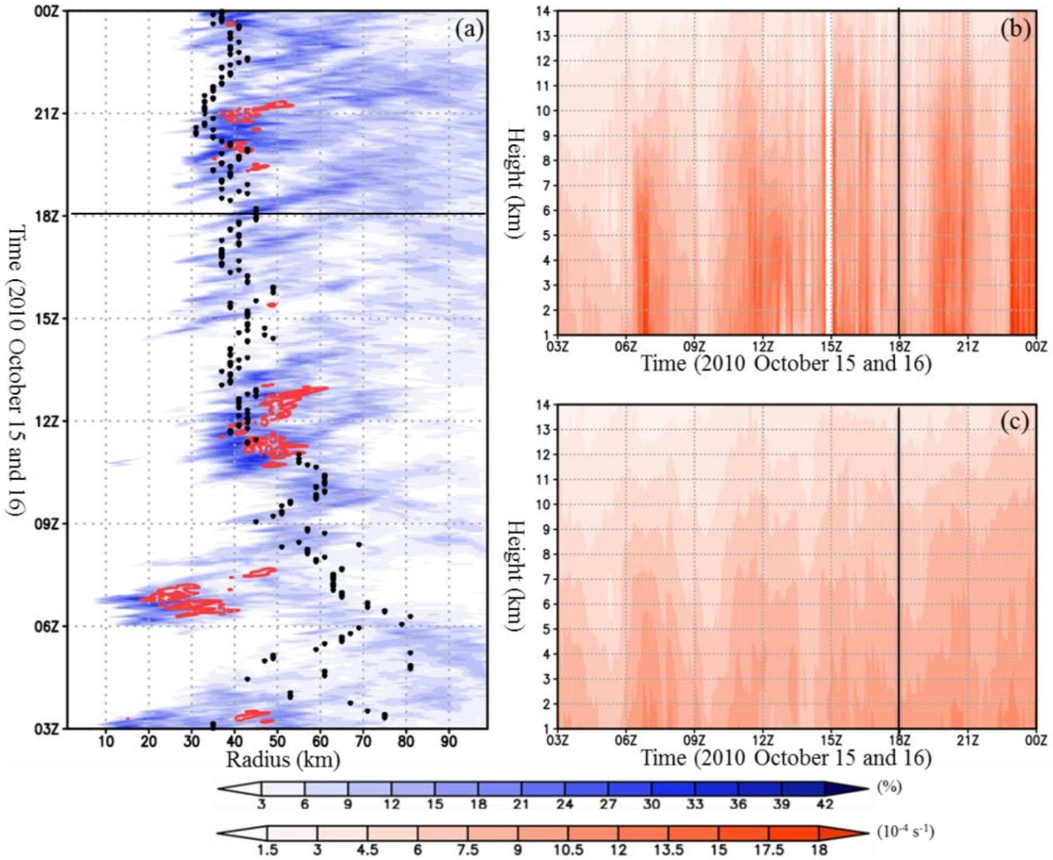

Figure 8. (a) The time-radius cross section of areal percentage accounted as weak-to-moderate convection (shaded, %) and CBs (red contour, at 5% interval) at different radius, overlaid with the RMW (black dots) at 7.5-km height. (b) The time-height cross section of averaged inertial stability (shaded, 10^{-4} s^{-1}) for grid points accounted as CBs within a radius of 80 km from the simulated TC center. (c) Same as in Fig. 8b, but is for weak-to-moderate convection.

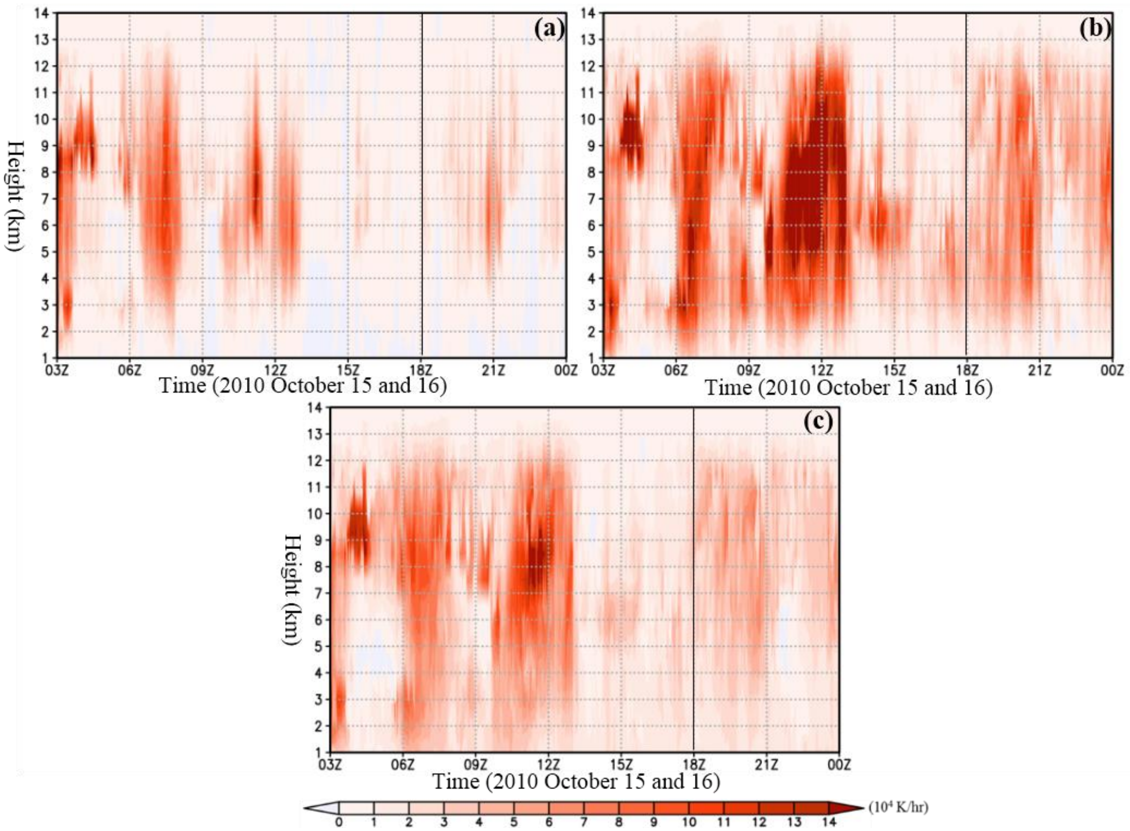

Figure 9. (a) The time-height cross section of the total latent heat (10^4 K hr^{-1}) contributed by CBs within the RMW. (b) Same as in Fig. 9a, but is for weak-to-moderate convection. (c) The time-height cross section of the total latent heat within the RMW.

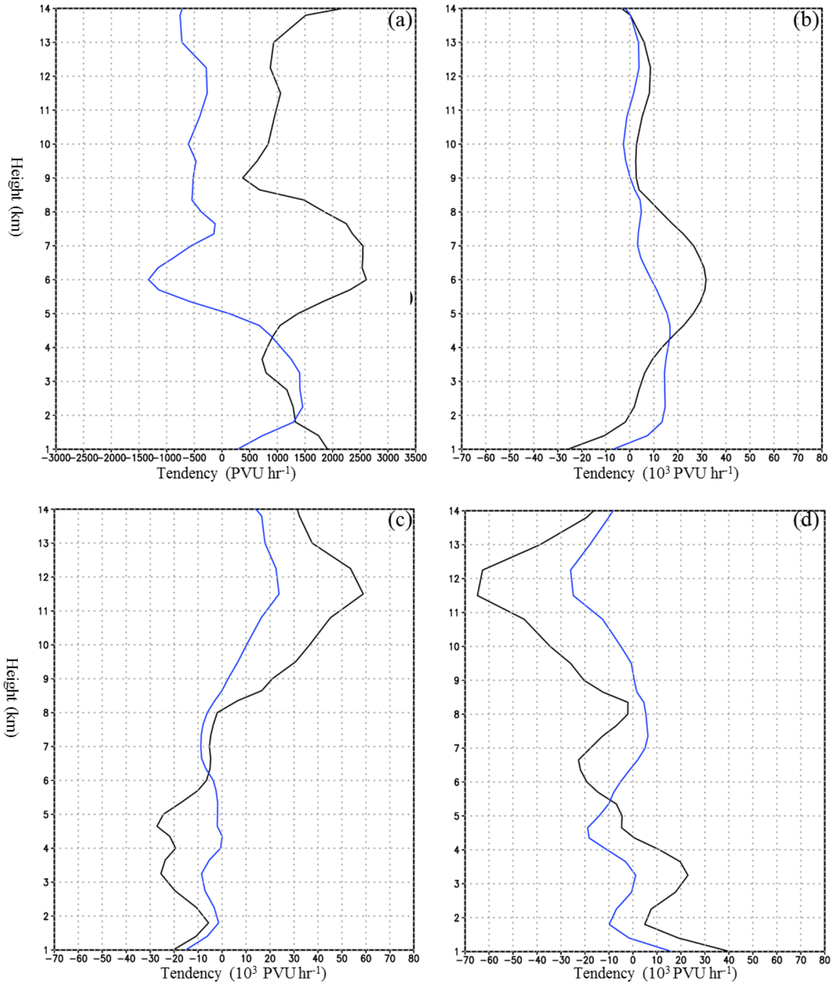

Figure 10. The height-PV tendency cross sections of (a) total PV tendency (PVU hr^{-1}) within a radius of 80 km from the simulated TC center. (b) Same as in Fig. 10a, but is for horizontal PV advection (10^3 PVU hr^{-1}). (c) Same as in Fig. 10a, but is for vertical PV advection (10^3 PVU hr^{-1}). (d) Same as in Fig. 10a, but is for heating induced PV (10^3 PVU hr^{-1}). Black lines denote the active CB phase. Blue lines denote the non-active CB phase.

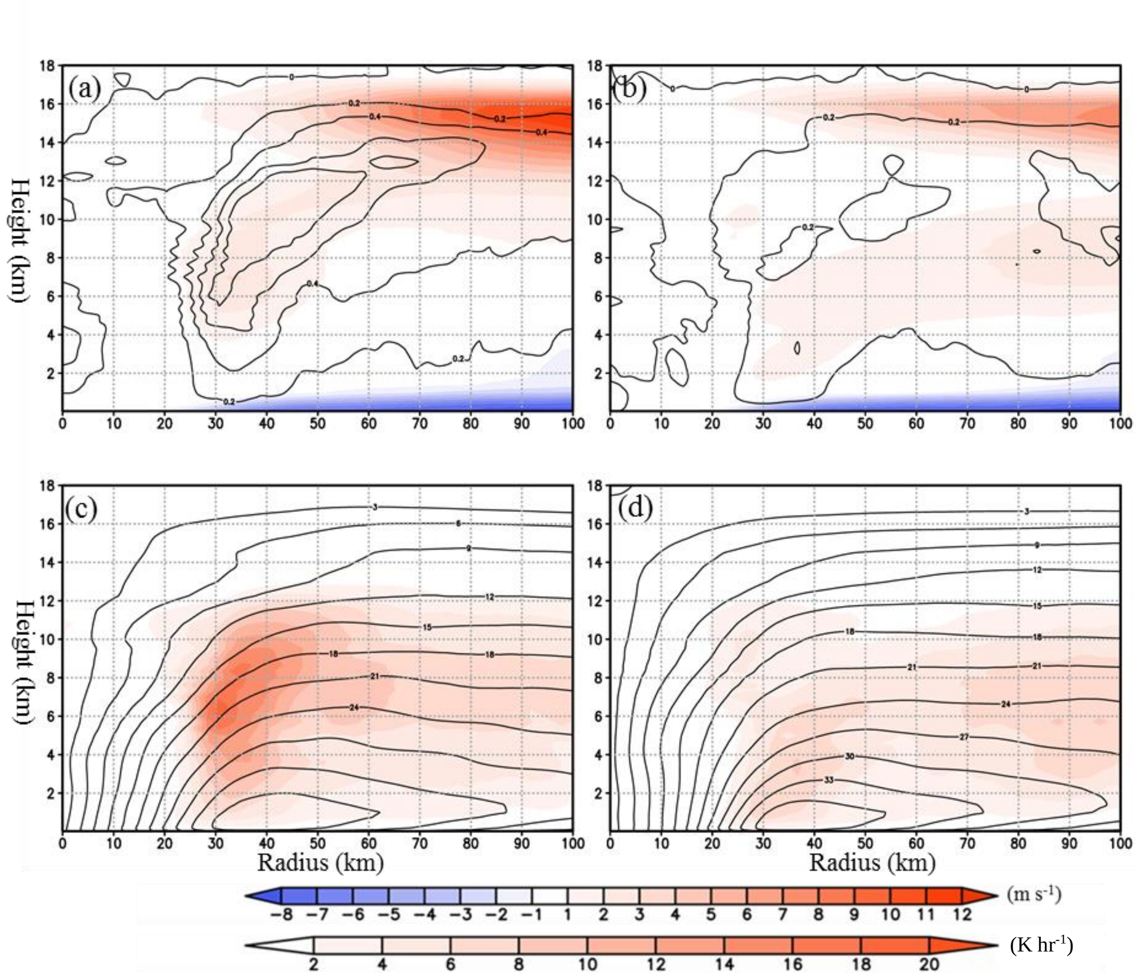

Figure 11. (a) The height-radius cross sections of time-averaged azimuthal mean radial wind (shaded, m s^{-1}) and vertical velocity (contours at 0.2–m s^{-1} intervals) during active CB phase. (b) Same as in Fig. 11a, but is for non-active CB phase. (c) The height-radius cross sections of time-averaged azimuthal mean latent heat (shaded, K hr^{-1}) and tangential wind (contours at 3–m s^{-1} intervals) during active CB phase. (d) Same as in Fig. 11c, but is for non-active CB phase.

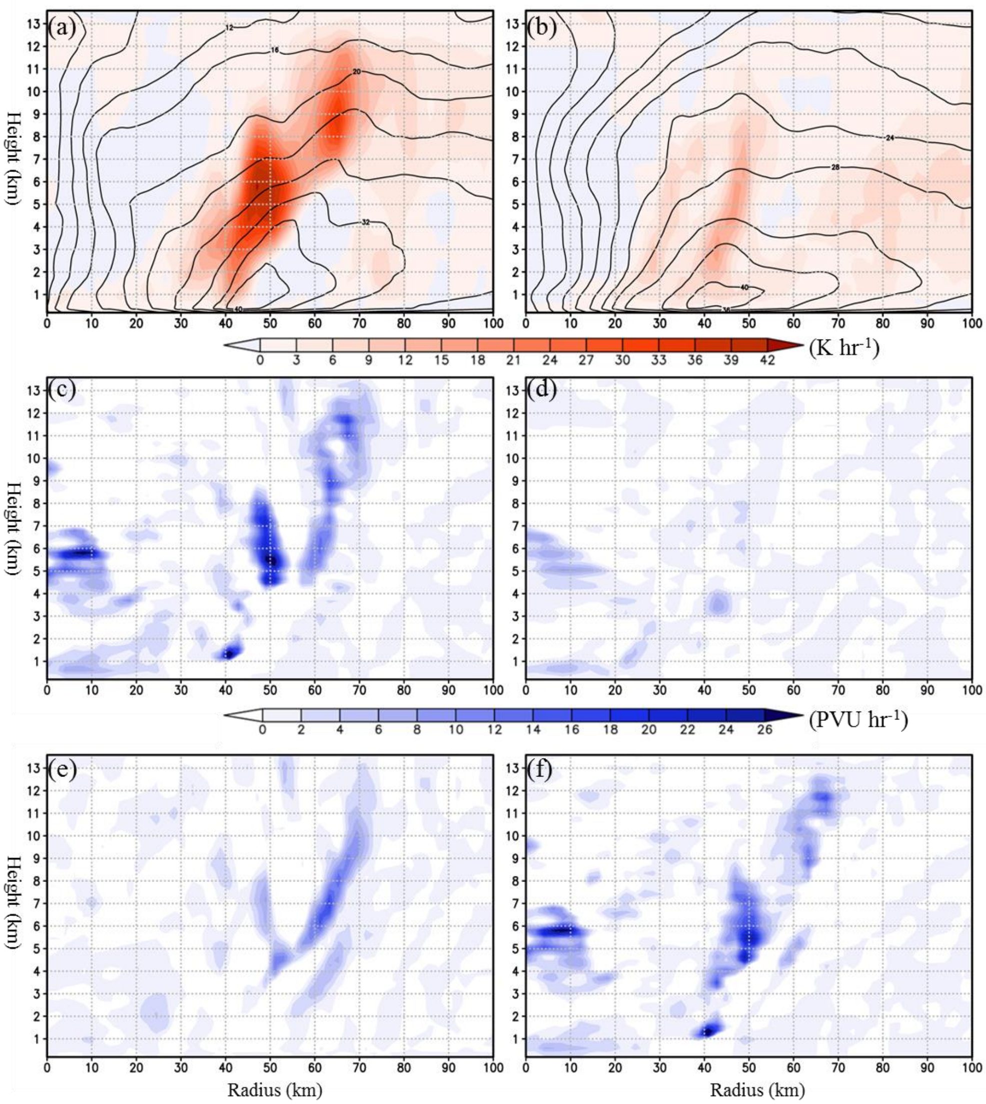

Figure 12. (a) The height-radius cross section of azimuthal mean latent heat (shaded, K hr^{-1}) and tangential wind (contours at 4-m s^{-1} intervals) at 1248 UTC 15 Oct, one moment of active CB phase. (b) Same as in Fig. 12a, but is for 1508 UTC 15 Oct, one moment of non-active CB phase. (c) The height-radius cross section of total PV advection (shaded, PVU hr^{-1}) due to the transverse circulation diagnosed by the SE model at 1248 UTC 15 Oct. (d) Same as in Fig. 12c, but is for 1508 UTC 15 Oct. (e) The height-radius cross section of PV advection (shaded, PVU hr^{-1}) due to the radial velocity

diagnosed by the SE model at 1248 UTC 15 Oct. (f) Same as in Fig. 12e, but is for vertical velocity.

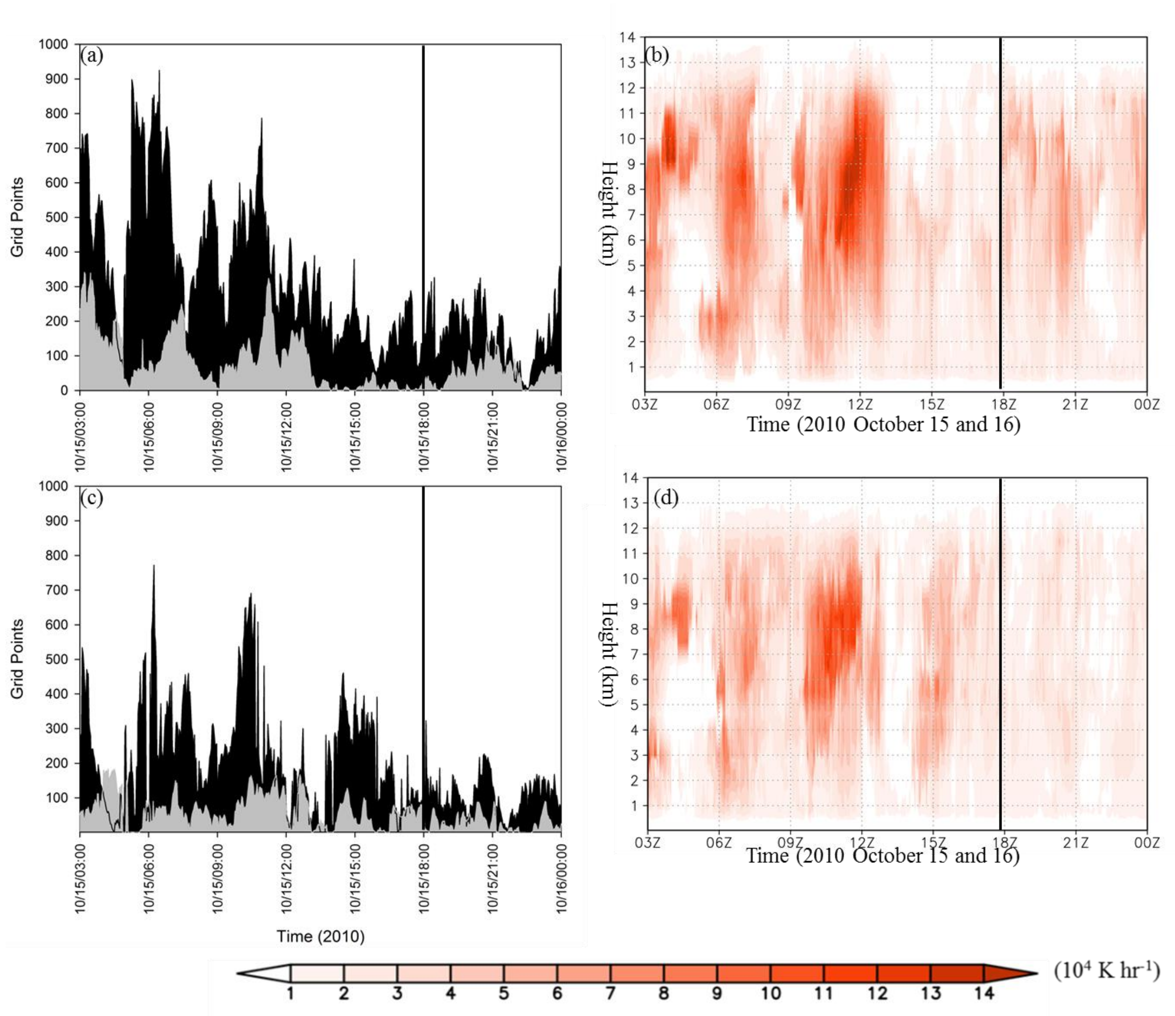

Figure 13. (a) Time series of the number of CB grid points (gray) within the RMW at 8-km height and the number of weak-to-moderate convection grid points (black) within the RMW at 3.35-km height for the CTRL experiment. (b) The time-height cross section of total latent heat (10^4 K hr^{-1}) within the RMW at different levels for the CTRL experiment. (c) Same as in Fig. 13a, but is for the WSM3 experiment. (d) Same as in Fig. 14b, but is for the WSM3 experiment. The thick black lines denote the onset of RI in the CTRL experiment.

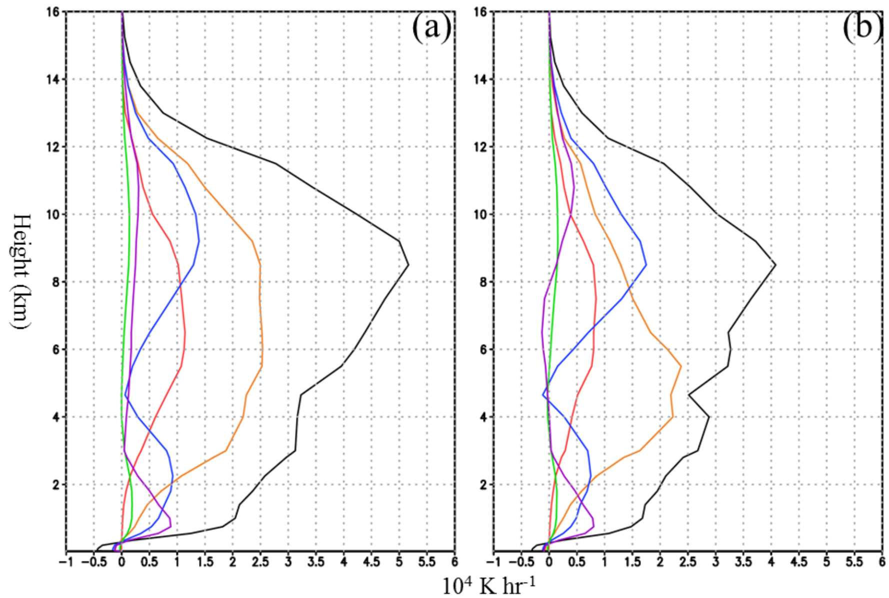

Figure 14. The time-averaged total latent heat inside the RMW (10^4 K hr^{-1}) contributed by different types of precipitation separated by the partitioning algorithm from Rogers (2010) for (a) CTRL and (b) WSM3 from 0300 UTC to 1800 UTC 15 October. The black lines denote the time-averaged total latent heat inside the RMW; the red lines the total latent heat contributed by CBs; the orange lines the total latent heat contributed by weak-to-moderate convection; the blue lines the total latent heat contributed by stratiform precipitation; the green lines the total latent heat contributed by other precipitation; and the purple lines the total latent heat contributed by no rain region.

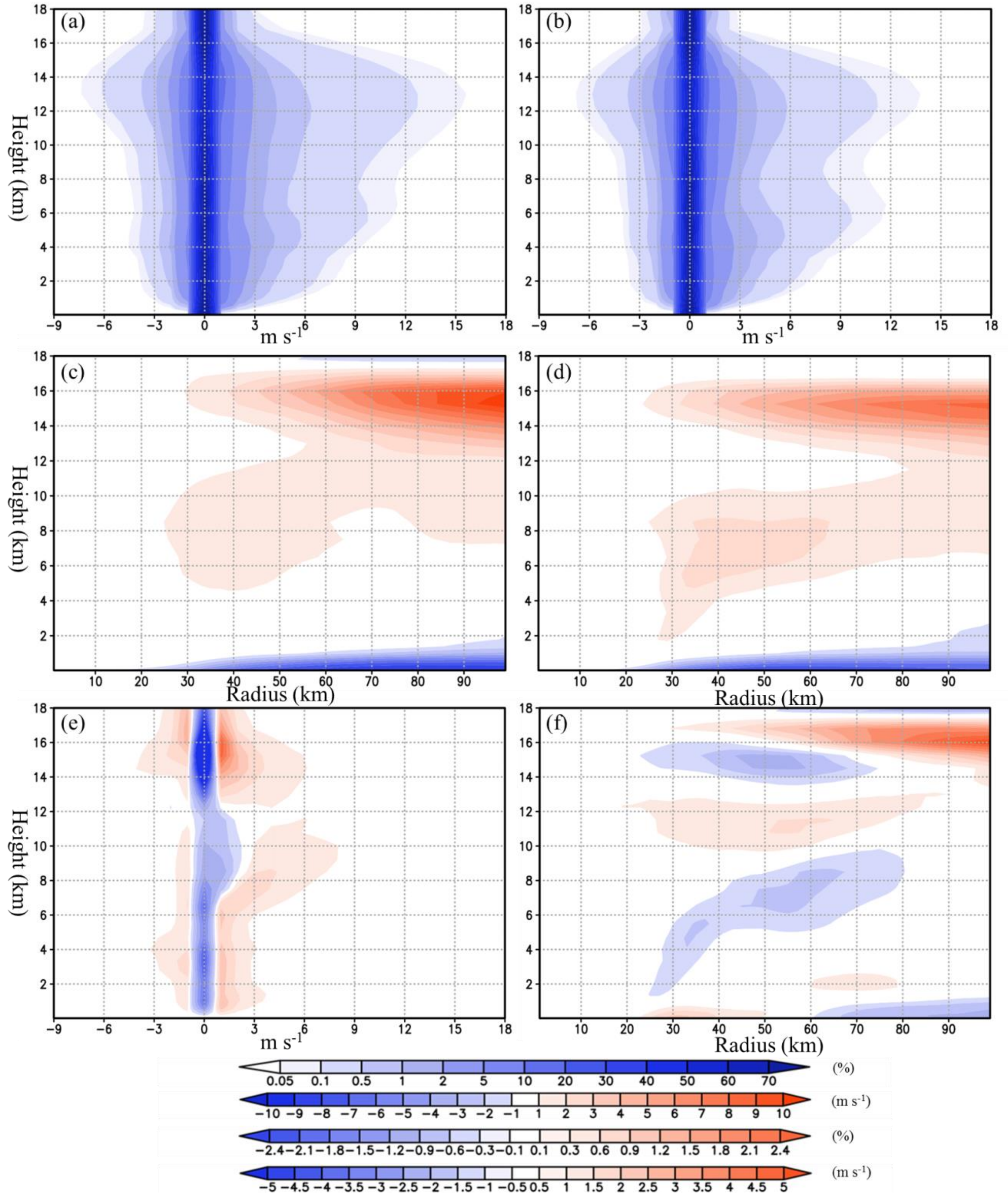

Figure 15. (a) The time-averaged CFDs of simulated vertical velocity (m s^{-1}) at each height between 0300 UTC and 1800 UTC 15 Oct for the CTRL experiment; contours represent frequencies (%) of the occurrence of vertical velocity within a radius of 80 km from the simulated TC center. (b) Same as in Fig. 14a, but is for the WSM3 experiment.

(c) The radius-height cross section of time-averaged azimuthal mean radial wind (m s^{-1}) between 0300 UTC and 1800 UTC 15 Oct for the CTRL experiment. (d) Same as in Fig. 14c, but is for the WSM3 experiment. (e) Difference of frequencies (%) plotted is the CFDs of vertical velocity for the CTRL experiment minus that for the WSM3 experiment. (f) Difference of wind speed (m s^{-1}) plotted is the azimuthal mean radial wind for the CTRL experiment minus that for the WSM3 experiment.

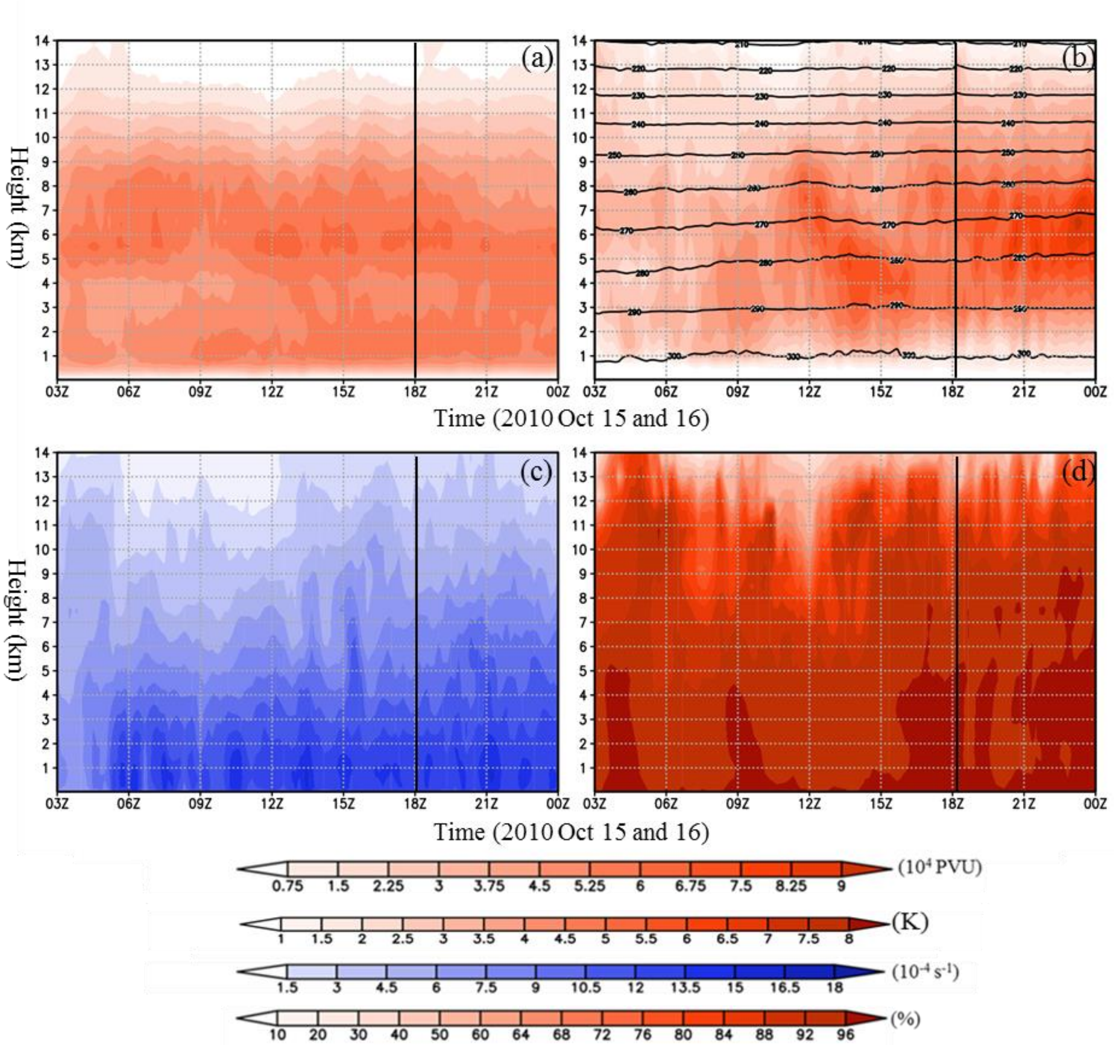

Figure 16. (a) The time-height cross section of total PV (10^4 PVU) within a radius of 80 km from the simulated TC center for the WSM3 experiment. (b) The time-height cross section of averaged Tv (K, contour) and Tv perturbation (K, shaded) within a radius of 20 km from the simulated TC center for the WSM3 experiment. (c) Same as in Fig. 15a, but is for mean inertial stability (10^{-4} s^{-1}). (d) The time-height cross section of mean axisymmetricity (%) within a radius between 20 and 80 km from the simulated TC center for the WSM3 experiment. The black lines denote the onset of RI in CTRL.

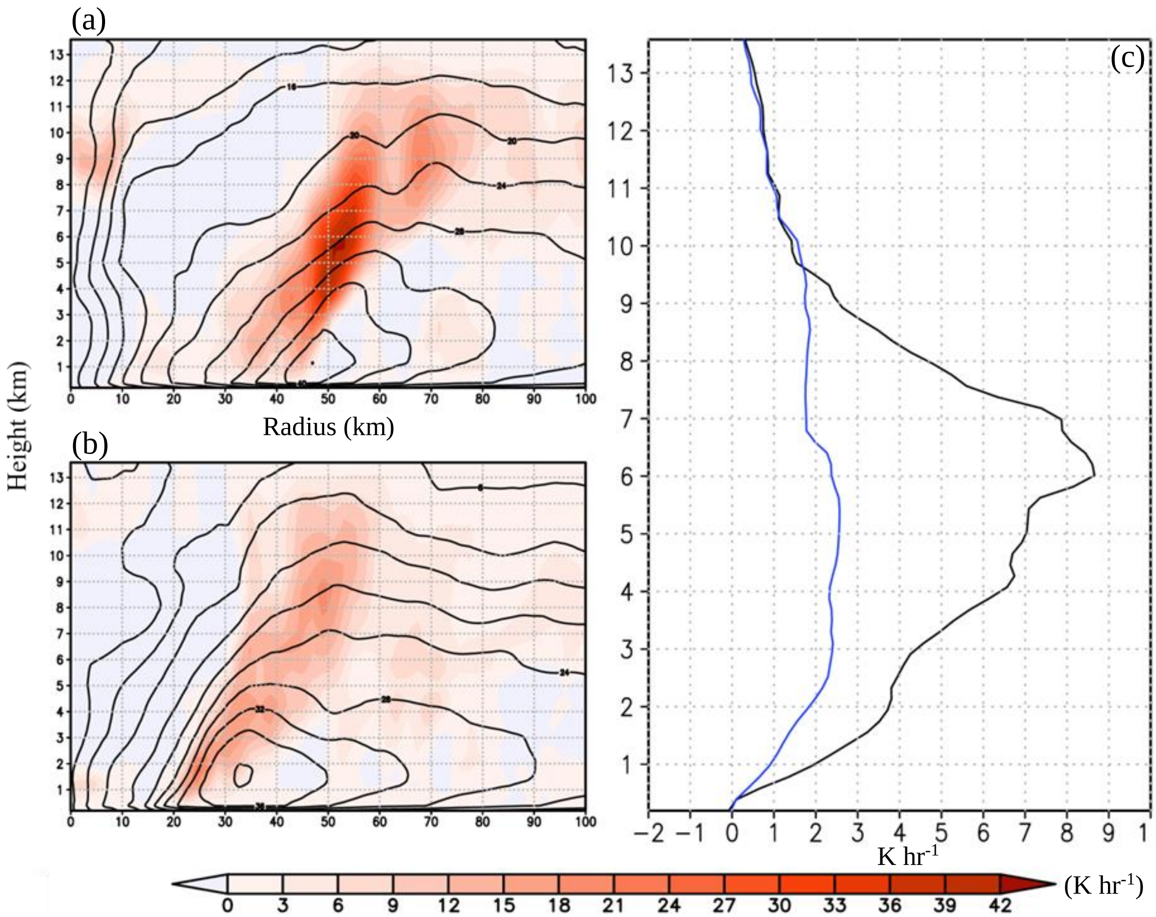

Figure17. (a) Same as in Fig. 12a. (b) Same as in Fig. 12b, but is for the WSM3 experiment. (c) The total θ advection (contour, K hr^{-1}) due to the transverse circulation diagnosed by the SE model at 1248 UTC 15 Oct for the CTRL experiment (black line) and the WSM3 experiment (blue line) within a radius of 20 km from the simulated TC center.

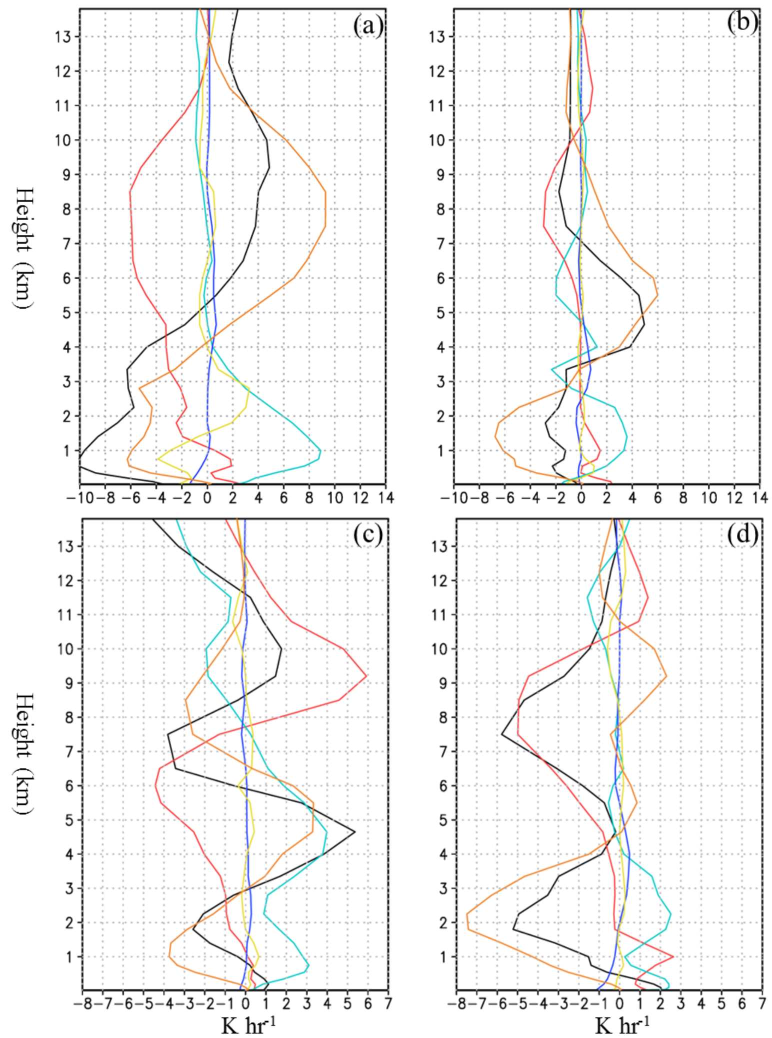

Figure 18. Each term in Eq. (6) for (a) CTRL experiment and (b) WSM3 experiment at 0800 UTC 15 Oct. The black lines indicate azimuthal mean θ tendency, the red lines the diabatic heating term (DH), yellow lines the θ tendency due to azimuthal mean radial θ advection**,** light-blue lines the θ tendency due ERAD, orange lines the θ tendency from MVAD, and blue lines the θ tendency caused by the eddy component of vertical θ advection. These terms are calculated at 2 min intervals on the height coordinates. (c) Same as in Fig. 17a, but is at 1248 UTC 15 Oct. (d) Same as in Fig. 17b, but is at 1248 UTC 15 Oct.

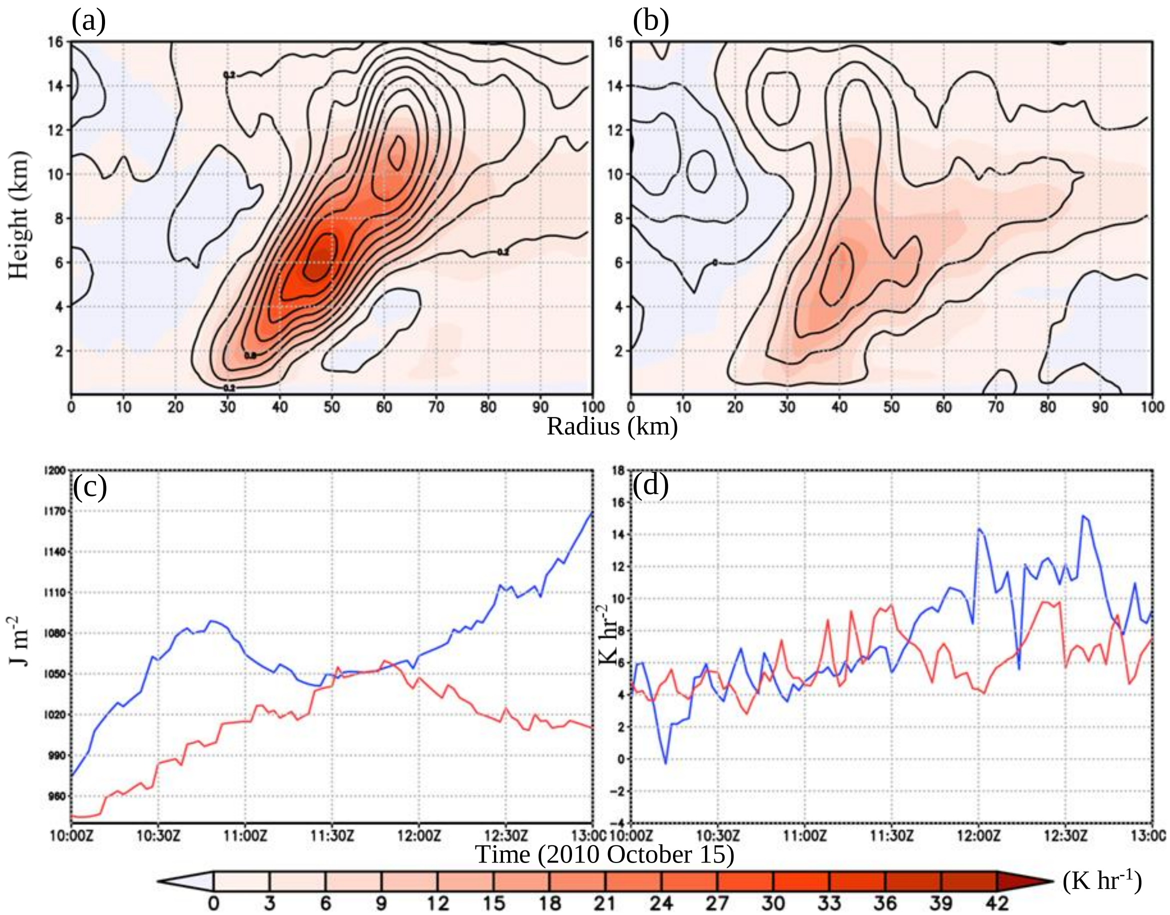

Figure 19. (a) The height-radius cross section of time-averaged azimuthal mean latent heat (shaded, K hr^{-1}) and vertical velocity (contours at 0.2-m s^{-1} intervals) during 1100 UTC and 1300 UTC 15 Oct for the CTRL experiment. (b) Same as in Fig. 19a, but is for the WSM3 experiment. (c) The time series of mean enthalpy fluxes (J m^{2}) within a radius of 80 km from the simulated TC center for the CTRL (blue line) and WSM3 (red line) experiments. (d) The time series of mean radial θ_e fluxes (K hr^{-1}) from the eye to eyewall at the radius of 30 km below 1-km height for the CTRL (blue line) and WSM3 (red line) experiments.

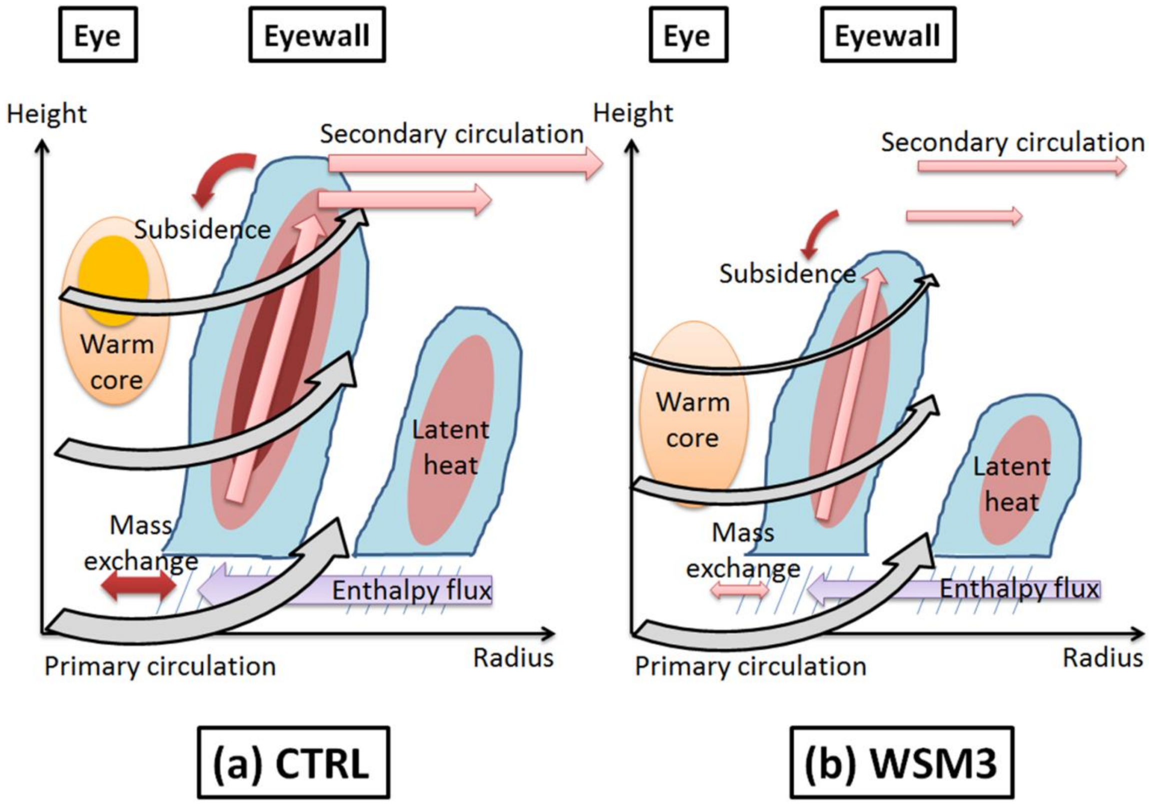

Figure 20. Schematics of radial distributions of inner-core convection, latent heat, primary circulation, secondary circulation, transportation of high-θ_e from the eye to eyewall, azimuthal mean subsidence, surface enthalpy flux and warm-core structure in (a) CTRL and (b) WSM3. CTRL has several distinct features prior to RI: more robust primary circulation and a warm core located at mid-upper level, resulted from the stronger secondary circulation. The more active convection with larger latent heat triggers the stronger secondary circulation. The larger surface enthalpy flux and transport of high-θ_e air from the eye to eyewall can be beneficial to the development of active inner-core convection.

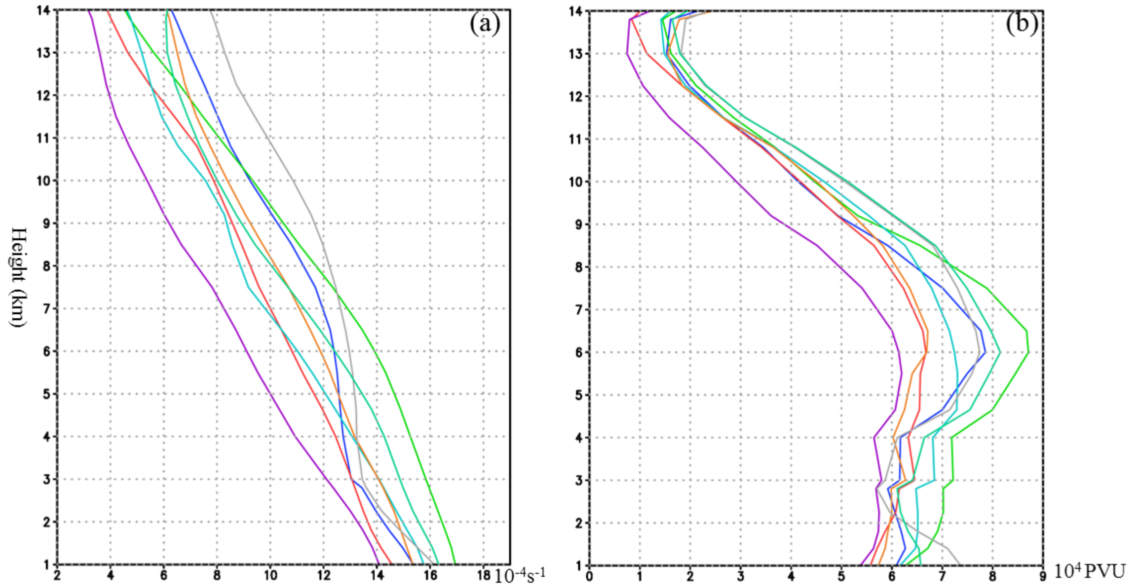

Figure B 1. (a) The time-averaged areal mean inertial stability (10^{-4} s^{-1}) within a radius of 80 km averaged from 3 h prior to RI onset for CTRL and other sensitivity experiments. (b) Same as in (a), but is for total PV (10^{4} PVU). The blue lines are CTRL, red lines Kessler, green lines Lin, purple lines WSM3, cyan lines WSM5, orange lines Ferr, grey lines WDM5 and aqua lines WDM6. Note that the onset times of intensification for each experiment are different, and WSM3 failed to undergo RI during the first 24 h of intensification.

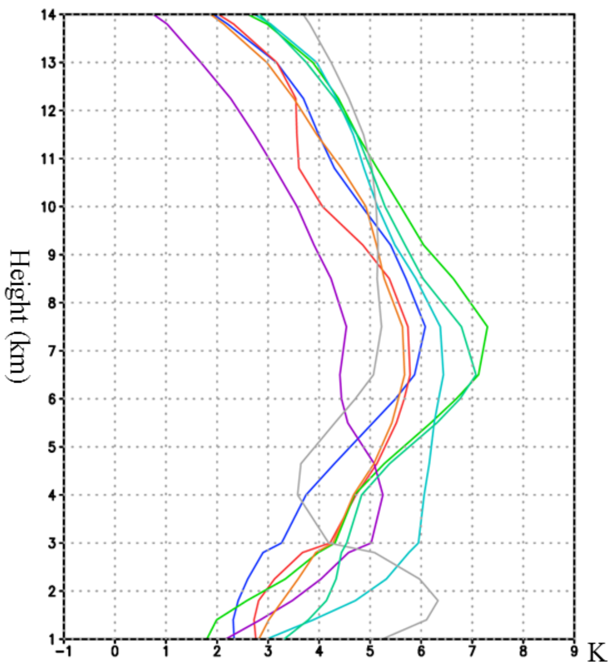

Figure B 2. (a) The time-averaged area-mean T_v perturbation (K) within a radius of 20 km averaged from 3 h prior to RI onset for CTRL and other sensitivity experiments. The blue lines are CTRL, red lines Kessler, green lines Lin, purple lines WSM3, cyan lines WSM5, orange lines Ferr, grey lines WDM5 and aqua lines WDM6. Note that the onset times of intensification for each experiment are different, and WSM3 failed to undergo RI during the first 24 h of intensification.

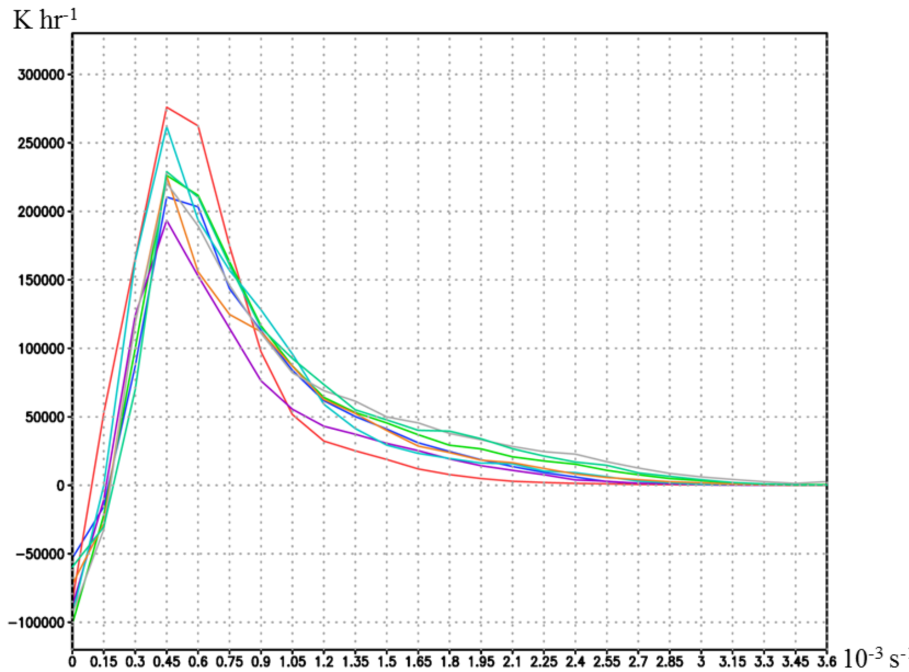

Figure B 3. (a) The time-averaged column-integrated total latent heat (K/hr) at different inertial stability values (10^{-3} s^{-1}) within a radius of 80 km averaged from 12 h prior to RI onset for CTRL and other sensitivity experiments. The blue lines are CTRL, red lines Kessler, green lines Lin, purple lines WSM3, cyan lines WSM5, orange lines Ferr, grey lines WDM5 and aqua lines WDM6. Note that the onset times of intensification for each experiment are different, and WSM3 failed to undergo RI during the first 24 h of intensification.

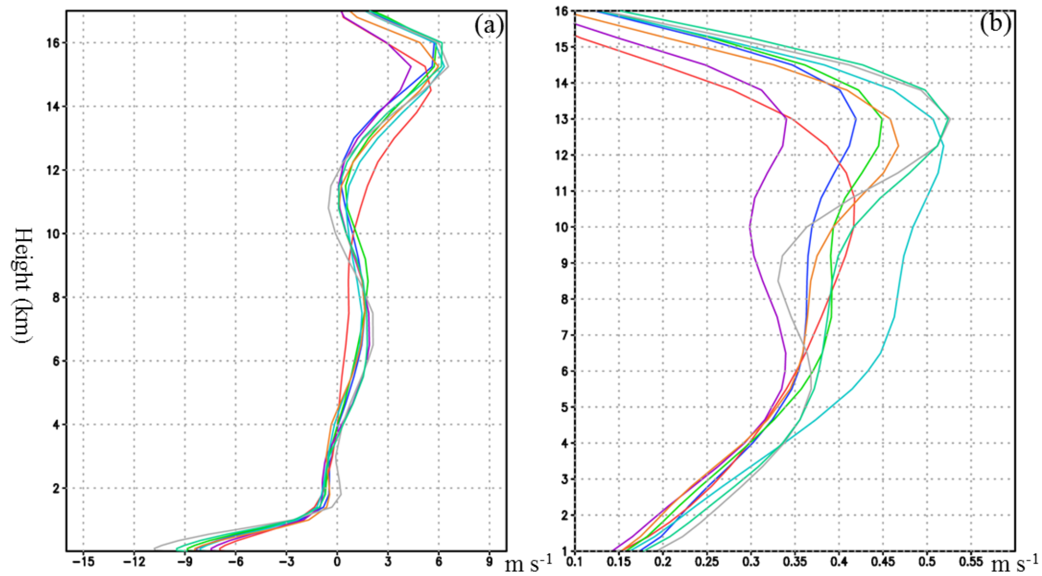

Figure B 4. (a) The time-averaged area-mean radial wind (m s^{-1}) within the radius between 30 to 100 km averaged from 12 h prior to RI onset for CTRL and other sensitivity experiments. (b) Same as in (a), but is for vertical velocity averaged within a radius of 80 km. The blue lines are CTRL, red lines Kessler, green lines Lin, purple lines WSM3, cyan lines WSM5, orange lines Ferr, grey lines WDM5 and aqua lines WDM6. Note that the onset times of intensification for each experiment are different, and WSM3 failed to undergo RI during the first 24 h of intensification.

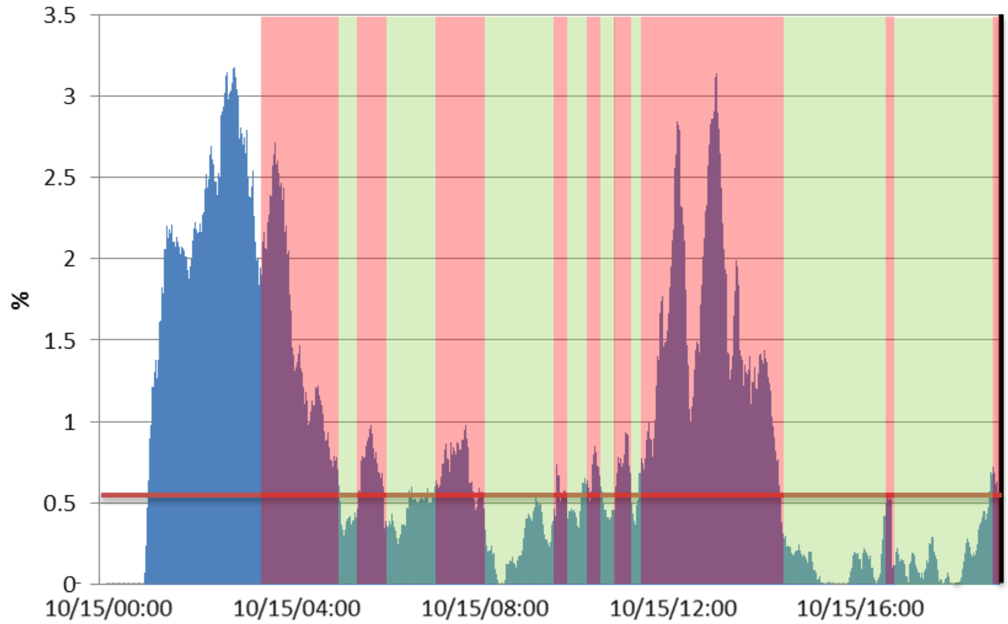

Figure E 1. Time series from 0000 UTC to 1800 UTC 15 October of the areal percentage (%) of CBs inside the radius of 80 km from the simulated center. The red line denotes 0.53 % of CB's areal ratio, and the black line denotes the onset of RI. The moments in red shadow are defined as "active CB phase", and the moments in green shadow are defined as "non-active CB phase".

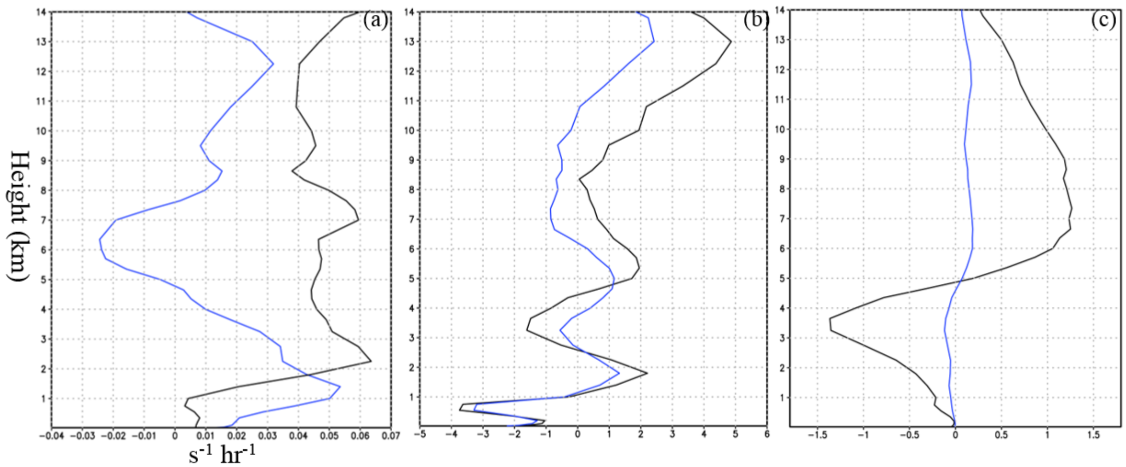

Figure G 1. The height-vorticity tendency cross sections of (a) total vorticity tendency (s^{-1} hr^{-1}) within a radius of 80 km. (b) Same as in Fig. R3-6a, but is for total vertical vorticity advection. (c) Total vertical vorticity advection (s^{-1} hr^{-1}) contributed by the CBs inside a radius of 80 km. Black lines denote the active CB phase. Blue lines denote the non-active CB phase.